Hyperspectral Image Denoising Using Local Low-Rank Matrix Recovery and Global Spatial–Spectral Total Variation

Wei He, *Member, IEEE*, Hongyan Zhang, *Senior Member, IEEE*, Huanfeng Shen, *Senior Member, IEEE*,
and Liangpei Zhang, *Senior Member, IEEE*

***Abstract*—Hyperspectral images (HSIs) are usually contaminated by various kinds of noise, such as stripes, deadlines, impulse noise, Gaussian noise, and so on, which significantly limits their subsequent application. In this paper, we model the stripes, deadlines, and impulse noise as sparse noise, and propose a unified mixed Gaussian noise and sparse noise removal framework named spatial–spectral total variation regularized local low-rank matrix recovery (LLRSSTV). The HSI is first divided into local overlapping patches, and rank-constrained low-rank matrix recovery is adopted to effectively separate the low-rank clean HSI patches from the sparse noise. Differing from the previous low-rank-based HSI denoising approaches, which process all the patches individually, a global spatial–spectral total variation regularized image reconstruction strategy is utilized to ensure the global spatial–spectral smoothness of the reconstructed image from the low-rank patches. In return, the globally reconstructed HSI further promotes the separation of the local low-rank components from the sparse noise. An augmented Lagrange multiplier method is adopted to solve the proposed LLRSSTV model, which simultaneously explores both the local low-rank property and the global spatial–spectral smoothness of the HSI. Both simulated and real HSI experiments were conducted to illustrate the advantage of the proposed method in HSI denoising, from visual/quantitative evaluations and time cost.**

***Index Terms*—Denoising, hyperspectral image (HSI), local low rank, mixed noise, spatial–spectral total variation (SSTV).**

I. INTRODUCTION

HYPERSPECTRAL image (HSI) data occupy an important place in the remote sensing community since they can provide hundreds of contiguous, narrow spectral bands. With the wealth of available spectral information, HSIs have been widely applied in food safety, pharmaceutical process monitoring and quality control, and biomedical, industrial, and forensic applications [1]. However, HSIs are unavoidably contaminated by various kinds of noise during the acquisition process, because of their unique physical design, which severely degrades the quality of the images and limits the precision of the subsequent processing tasks, such as classification, unmixing, target detection, and so on [1]–[4]. Therefore, as a preprocessing step of the HSI image application, denoising is an active and challenging research topic.

HSIs contain two spatial dimensions (along the track and across the track) and one spectral dimension (wavelength) [5], [6]. Generally speaking, an HSI is an extension of an RGB image, and it contains hundreds of bands sampled from the visible and infrared range of the electromagnetic spectrum. If we treat each band of an HSI as a gray-level image, many of the state-of-the-art gray-level image denoising methods [7]–[10] can be adopted to denoise the HSI in a band-by-band manner. However, this kind of processing method ignores the high correlations between the different spectral bands and often results in a relatively low-quality result. As mentioned in many studies [11]–[14], spectral redundancy and correlation is also important for HSI denoising and restoration. As a result, spatial–spectral redundancy and correlation is a unique characteristic of HSIs, and it has resulted in many specially designed methods for HSI denoising. Notably, there are two challenges for HSI denoising. One is that the noise intensity of the different bands is often different [15]. Typically, most bands of an HSI are of high quality; meanwhile, some specific bands may be corrupted by heavy noise. This results in the challenge of how to effectively preserve the high signal-to-noise ratio (SNR) bands while denoising the low-SNR bands. The second challenge is the existence of mixed noise in HSIs, which are often simultaneously contaminated by stripes, deadlines [5], impulse noise, Gaussian noise [16], and so on. The statistical characteristics of the different types of noise are different, resulting in a new barrier to the denoising of HSIs. The goal of this work is to remove the mixed noise of HSIs before the subsequent interpretation task.

In the past two decades, various methods have been proposed for HSI data noise removal [17]–[20]. In this paper, we focus on the total variation (TV) and low-rank-based HSI denoising

---

Manuscript received May 31, 2017; revised October 30, 2017 and January 6, 2018; accepted January 28, 2018. Date of current version March 9, 2018. This work was supported in part by the National Natural Science Foundation of China under Grant 41571362, Grant 41711530709, and Grant 41431175, and in part by the Major Special Project of the China High Resolution Earth Observation System. *(Corresponding authors: Hongyan Zhang and Liangpei Zhang.)*

W. He, H. Zhang, and L. Zhang are with the State Key Laboratory of Information Engineering in Surveying, Mapping, and Remote Sensing, and the Collaborative Innovation Center of Geospatial Technology, Wuhan University, Wuhan 430072, China (e-mail: weihe1990@whu.edu.cn; zhanghongyan@whu.edu.cn; zlp62@whu.edu.cn).

H. Shen is with the School of Resource and Environmental Sciences, Wuhan University, Wuhan 430072, China (e-mail: shenhf@whu.edu.cn).

Color versions of one or more of the figures in this paper are available online at http://ieeexplore.ieee.org.

Digital Object Identifier 10.1109/JSTARS.2018.2800701

methods and give a brief review of the existing popular methods below. TV regularization is a powerful model in image processing and was first proposed by Rudin *et al.* [56] to solve the gray-level image denoising problem because of its ability to effectively preserve edge information and promote piecewise smoothness. In [22], TV regularization was further developed into the color image restoration problem, and a color TV model was proposed. Compared to color images, HSIs have hundreds of bands and the noise intensity of the different bands is often different [15]. To better suppress the noise in the high noise intensity bands while preserving the detailed information in the low noise intensity bands, the denoising strength should be adaptively adjusted to the noise intensity in the different bands. Based on this criterion, Yuan *et al.* [23] proposed an HSI restoration algorithm employing a spectral–spatial adaptive TV (SSAHTV) model. In [5], Chang *et al.* proposed to treat the HSI as a spatial–spectral volume [25] and proposed anisotropic spatial–spectral total variation (SSTV) regularization to enhance the smoothness of the solution along both the spectral and spatial dimensions. In this way, both the consistent spectral information in the spectral dimension and the spatial piecewise smooth information in the spatial dimension are promoted and the restoration result is significantly improved. Notably, despite their good performance in single-type noise removal, the TV-regularized methods cannot remove mixed noise in HSIs.

Low-rank matrix/tensor approximation is another powerful tool in image processing. It describes the problem of finding and exploiting low-dimensional structures in high-dimensional data and has been widely used in the image denoising problem to separate the low-dimensional signal from the high-dimensional noise [21], [24], [26]. For a scene of a clean HSI, it is usually assumed to be composed of only a few endmembers, which are far fewer than the number of spectral bands and pixels [1], [27], revealing the low-rank structure of the hyperspectral imagery. Based on this fact, principal component analysis (PCA) [13], low-rank tensor approximation [28], and low-rank matrix factorization based methods have been successfully adopted to denoise HSIs. Unfortunately, these classical methods have two major drawbacks. First, these methods are sensitive to outliers [21]; however, HSIs are often contaminated by outliers such as stripes, deadlines, impulse noise, and so on. Second, these methods can perform well only when the image is corrupted by a small amount of Gaussian noise. When the image is contaminated by heavy Gaussian noise, the obtained low-dimensional signal will also be corrupted by noise. In [21], Candès *et al.* proposed the robust PCA (RPCA) model and solved the first problem. They modeled the outliers and Gaussian noise separately, and proved that, under certain conditions, there is a high probability of recovering the low-rank matrix from the observed data corrupted by mixed noise. The RPCA model and its variations have been successfully used in HSI mixed-noise removal [14], [29], [30]–[32], achieving state-of-the-art results.

For the second problem, there are two main approaches. The low-rank-based denoising methods only explore the correlation between spectral bands, ignoring the spatial correlation of local neighborhood pixels. Naturally, the first approach is to incorporate the spatial information in the low-rank model by simultaneously utilizing both the spectral and spatial information. Several tools have been utilized in low-rank models to denoise HSIs, including wavelets [33], [34], TV regularization [35], [37], [47], [48], sparse representation [36], and so on, and have also achieved state-of-the-art results. One notable fact is that all these methods model the whole HSI as low rank and impose reasonable regularization constraints on the whole image. From another aspect, the spectral signatures of the same material from different local areas may be significantly different, showing the spectral variability of HSIs. The existence of spectral variability can destroy the global low-rank property of HSIs, to some extent, and can result in performance degradation of the low-rank-based denoising methods. Fortunately, pixels from the same local area are more likely to be the same material, and the spectral signatures of the same material are more likely to be the same. That is to say, if we model the HSI locally, the low-rank property can be effectively enhanced. Based on this fact, Zhang *et al*. [14] and Xie *et al*. [38] first segmented the HSI into overlapping 3-D patches, and then used the RPCA model to process each patch sequentially. To more efficiently group the spatial–spectral similar pixels, Lu *et al.* [39] introduced a spatially adaptive local similar pixel search method to adaptively select the patches. The same idea was also introduced in [40], where the Markov random field method was used to segment the HSI into patches. Besides the low-rank modeling of local patches, the nonlocal similarity of patches has also been adopted to further improve the performance of HSI denoising [41], [42]. The basic idea of this kind of method is that it is more effective to model the HSI with a local low-rank structure to remove the mixed noise. Unfortunately, these local low-rank-based methods cannot remove the structured sparse noise (i.e., the sparse noise existing in the same location of some bands or even all the bands), so it is necessary to use a spatial constraint to remove the structured sparse noise.

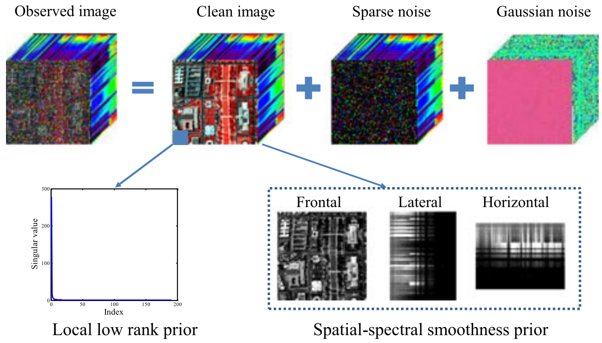

Fig. 1. HSI degradation model and the priors of a clean HSI.

The degradation of the observed HSI and the priors are presented in Fig. 1. Following the idea of [14], we model the impulse noise, dead pixels, and stripes as sparse noise, and the desired clean HSI underlies the local low-rank structure, as shown in Fig. 1. Furthermore, from the frontal, lateral, and horizontal views, the desired clean HSI also exhibits global piecewise smoothness from the spatial view and spectral consistency from the spectral perspective. To sum up, it is essential to build a unified framework and simultaneously benefit from the local low-rank structure and the global spatial–spectral piecewise smoothness and consistency.

In light of the above-mentioned arguments, we propose the SSTV-regularized local low-rank matrix recovery (LLRSSTV) method for HSI denoising. The HSI data are first divided into overlapping patches and a rank-constrained local low-rank-based method is adopted to separate the low-rank components from each noisy patch sequentially. In this way, the sparse noise can be effectively separated from the HSI data. Unfortunately, the low-rank components may still be corrupted by a small amount of Gaussian noise. SSTV is then used to reconstruct these low-rank patches of the image, to further remove the noise by capturing the global smoothness of the HSI. In return, the reconstructed image is fed back to help the local low-rank and sparse decomposition in the first step. The main contribution of this paper is that this is the first time that a global SSTV regularization model has been adopted to reconstruct the denoised low-rank patches in HSI denoising. Recently, the patch-based processing strategy has become a hot topic in image denoising and restoration [8], [10], [14]. Most of these works have reconstructed the denoised patches in a simple way, where the final output of each pixel is the weighted average across multiple patches containing the pixel. Here, we assume that the reconstructed image enjoys global spatial–spectral smoothness, and we adopt the SSTV model to reconstruct these denoised patches. Thus, the desired local and global properties of the HSI are integrated. From the local perspective, the rank-constrained low-rank matrix recovery is adopted to effectively separate the low-rank components from the sparse noise. As to the global perspective, SSTV is utilized to explore the global spatial–spectral piecewise smoothness and consistency of the HSI. The experimental results confirm that the proposed method clearly improves the denoising results when compared with some of the state-of-the-art techniques, in both the quantitative evaluations and the visual comparisons.

The rest of this paper is organized as follows. In Section II, the proposed model is introduced. The optimization procedure is presented in Section III. Both simulated and real HSI data experiments are described and analyzed in Section IV. Finally, the conclusions are drawn in Section V.

II. RELATED WORK

A. Problem Formulation

In general, HSIs are assumed to be corrupted by a mixture of different kinds of noise, which typically consists of Gaussian noise, impulse noise, dead pixels or lines, and stripes [14]. The degradation of an HSI can be modeled as

$$\mathcal{O} = \mathcal{L} + \mathcal{S} + \mathcal{N} \tag{1}$$

where $\mathcal{O}$ represents the observed corrupted HSI; $\mathcal{L}$ is the latent clean HSI; $\mathcal{S}$ denotes the sparse noise, which contains impulse noise, deadlines, and stripes; and $\mathcal{N}$ is the Gaussian noise. All the images $\mathcal{O}, \mathcal{L}, \mathcal{S}$, and $\mathcal{N}$ are of the same size, i.e., $M \times N \times p$, where $M \times N$ is the spatial size of the HSI and p is the number of bands. The purpose of HSI denoising is to estimate the clean image $\mathcal{L}$ from the noisy observation $\mathcal{O}$.

B. SSTV-Based Regularization

TV-based regularization was first proposed in [56] and has since been widely used in HSI processing [5], [23], [35] due to its desirable properties, such as convexity and the ability to capture the global piecewise smoothness structure. The TV norm can be either an anisotropic TV norm or an isotropic TV norm [25]. For HSI noise removal, obvious blurring artifacts can be easily introduced by the isotropic model [5], inspiring us to focus on the investigation of the anisotropic TV norm [19]. For a gray-level image $\boldsymbol{u}$ of size $M \times N$, the anisotropic TV norm is defined as

$$||u||_{\mathrm{TV}} = \|\mathbf{D}_i u\|_1 + \|\mathbf{D}_j u\|_1 \tag{2}$$

where $\mathbf{D}_i$ and $\mathbf{D}_j$ are linear operators corresponding to the horizontal and vertical first-order discrete differences, respectively. This model can be easily extended to an HSI in a band-by-band manner. That is to say, every band of the HSI is treated as a gray-level image. The TV norm (2) is then applied to each band, and then added together [23], [35]. However, this band-by-band TV model only explores the spatial smoothness, ignoring the high correlation of the spectral signatures and the gray-level images of each band [48]. For an HSI, two nearby band images are usually very similar, indicating spectral consistency. Therefore, it can be argued that the noise can be removed by simultaneously enforcing both spatial piecewise smoothness and spectral consistency. For a 3-D observed HSI cube $\mathcal{L}$, the anisotropic spatial–spectral TV norm can be formulated as

$$\|\mathcal{L}\|_{\mathrm{SSTV}} = \|\mathbf{D}_i \mathcal{L}\|_1 + \|\mathbf{D}_j \mathcal{L}\|_1 + \|\mathbf{D}_b \mathcal{L}\|_1 \tag{3}$$

where $\mathbf{D}_b$ is the forward finite-difference operator along the spectral direction. The definitions of operators $\mathbf{D}_i$, $\mathbf{D}_j$, and $\mathbf{D}_b$ are

$$\begin{cases} \mathbf{D}_i \mathcal{L} = \mathcal{L}(i+1, j, b) - \mathcal{L}(i, j, b) \\ \mathbf{D}_j \mathcal{L} = \mathcal{L}(i, j+1, b) - \mathcal{L}(i, j, b) \\ \mathbf{D}_b \mathcal{L} = \mathcal{L}(i, j, b+1) - \mathcal{L}(i, j, b) \end{cases} \tag{4}$$

with periodic boundary conditions.

By using the regularization (3), the piecewise smoothness structure in both the spatial and spectral directions can be explored. This model treats the gradient of each dimension equally. However, the intensity of the gradient in the different directions may not be the same. Fig. 2 shows the gradient image of the HSI cube in the three different directions. We, therefore, extend (3) to the following anisotropic SSTV regularization:

$$\|\mathcal{L}\|_{\mathrm{SSTV}} = \tau_i \|\mathbf{D}_i \mathcal{L}\|_1 + \tau_j \|\mathbf{D}_j \mathcal{L}\|_1 + \tau_b \|\mathbf{D}_b \mathcal{L}\|_1 \tag{5}$$

where τ_i, τ_j, and τ_b are three regularization parameters to tradeoff the contribution of the gradient norm in the different directions. We adopt the observation made in [25] and set $\tau_i = \tau_j = 1$, which means that the two spatial dimensions make the same contribution to the SSTV regularization.

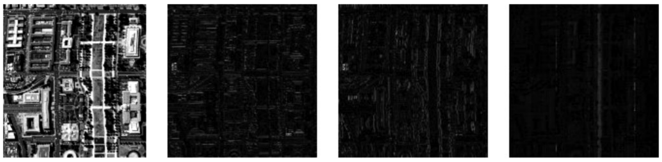

(a) (b) (c) (d)

Fig. 2. Gradient images of the HSI cube in three different directions. (a) Original image. (b) The gradient image from the spatial i-direction; (c) the gradient image from the spatial j-direction; and (d) the gradient image from the spectral direction.

III. Proposed Method

A. Local Low-Rank-Based HSI Denoising

Spectrally adjacent bands of an HSI typically exhibit strong correlations, and spatially adjacent pixels in the HSI are also typically highly correlated, which both reveal the low-rank structure of hyperspectral imagery. From a linear mixture model perspective [1], the corresponding clean HSI $\mathbf{L}$ can be expressed as $\mathbf{L} = \mathbf{AM}$, where $\mathbf{L} \in \mathbb{R}^{MN\times p}$ is the Casorati matrix (a matrix whose columns comprise vectorized bands of the HSI) of clean HSI $\mathcal{L}$; $\mathbf{A} \in \mathbb{R}^{MN\times r}$ and $\mathbf{M} \in \mathbb{R}^{r\times p}$ are the low-rank factorization matrices of the matrix $\mathbf{L}$; and r is the dimension of the signal subspace. Immediately, the exploration of clean matrix $\mathbf{L}$ can be formulated as the following rank-constrained RPCA optimization problem [35]:

$$\min_{\mathbf{L},\mathbf{S}} ||\mathbf{L}||_* + \lambda||\mathbf{S}||_1, \ \text{s.t.}, \ ||\mathbf{O} - \mathbf{L} - \mathbf{S}||_F^2 \leq \varepsilon, \ \text{rank}\,(\mathbf{L}) \leq r \tag{6}$$

where $\mathbf{O}$, $\mathbf{S}$, and $\mathbf{N}$ are the Casorati matrices of observed image $\mathcal{O}$, sparse noise $\mathcal{S}$, and Gaussian noise $\mathcal{N}$, respectively. λ is the sparsity regularization parameter. $\|\mathbf{L}\|_*$ is the nuclear norm, i.e., the sum of the singular values of matrix $\mathbf{L}$. For the derivation of the optimization (6), we refer the reader to our previous paper [35].

Model (6) can now be directly used in the mixed-noise removal of HSIs. However, considering that matrix $\mathbf{O}$ has a size of $MN \times p$, the spatial dimensionality greatly exceeds the spectral dimensionality $(MN \gg p)$, and $\mathbf{O}$ is typically a very thin matrix. In this case, the denoised image by rank-constrained RPCA may result in blurring and a loss of details [46]. Fortunately, pixels from the same local area are more likely to be the same material, and the spectral signatures of the same material are more likely to be the same. This inspires us to explore the local low-rank property of the HSI; that is to say, we analyze the HSI in a spatial patch-wise manner, rather than globally, as in [14] and [41]. Thus, we divide the HSI into overlapping patches and exploit the patch-level local low-rank structure.

We define an operator $R_{i,j} : \mathcal{L} \rightarrow \mathbf{L}_{i,j}$, where $R_{i,j}$ is a binary operator that extracts $m \times n$ rows from an $m \times n \times p$ patch cube centralized at location $(i,\, j)$ of the HSI, and $\mathbf{L}_{i,j}$ denotes the corresponding Casorati matrix. We use $\mathcal{L}_{i,j}$ to denote the result of operation $R_{i,j}$ on the tensor $\mathcal{L}$, i.e., $\mathcal{L}_{i,j} = R_{i,j}(\mathcal{L}) = \mathbf{L}_{i,j}$. By this definition, for each patch matrix $\mathbf{O}_{i,j}$, model (6) is adopted to extract $\mathbf{L}_{i,j}$ and $\mathbf{S}_{i,j}$. Thus, the local patch-based rank-constrained RPCA model can be described as

$$\min_{\mathcal{L},\mathcal{S}} \sum_{(i,j)\in[1,M-m+1]\times[1,N-n+1]} (||\mathcal{L}_{i,j}||_* + \lambda||\mathcal{S}_{i,j}||_1)$$
$$\text{s.t.}, \ ||\mathcal{O}_{i,j} - \mathcal{L}_{i,j} - \mathcal{S}_{i,j}||_F^2 \leq \varepsilon, \ \text{rank}\,(\mathcal{L}_{i,j}) \leq r. \tag{7}$$

Here, we assume that r is the upper bound of the signal dimension for all the patches. The patch-wise RPCA model (7) has been applied to HSI denoising with different algorithm solutions [14], [38]. However, differing from the previous approaches in which each patch is denoised individually, we treat all the patches globally and update them simultaneously.

B. SSTV-Regularized Local Low-Rank (LLRSSTV)-Based HSI Denoising

Patch-based local low-rank methods have achieved great success in HSI denoising [14], [38], [41], [42]. These low-rank-based methods investigate the spectral similarity of the HSI and have a great advantage when faced with random sparse noise and Gaussian noise separation. However, when the sparse noise is structured, i.e., the sparse noise exists in the same location of some HSI bands or even all the bands, the separation performance for the sparse noise and Gaussian noise will be severely degraded. In addition, when the Gaussian noise is heavy, the removal of the noise will also be influenced. Thus, spatial information exploration is also important in the low-rank-based denoising methods.

By embedding this SSTV regularization (5) into the local patch-based rank-constrained RPCA model (7), the proposed LLRSSTV model can be described as

$$\min_{\mathcal{L},\mathcal{S}} \sum\nolimits_{i,j} (||\mathcal{L}_{i,j}||_* + \lambda||\mathcal{S}_{i,j}||_1) + \tau||\mathcal{L}||_{\text{SSTV}}$$
$$\text{s.t.}, \ ||\mathcal{O}_{i,j} - \mathcal{L}_{i,j} - \mathcal{S}_{i,j}||_F^2 \leq \varepsilon, \ \text{rank}\,(\mathcal{L}_{i,j}) \leq r \tag{8}$$

where λ and τ are the regularization parameters.

It should be noted that, in the proposed LLRSSTV model, the local low-rank and sparse matrix decomposition is implemented in the local patches simultaneously to better separate the sparse noise and the heavy Gaussian noise from the local low-rank clean patches by exploiting the local low-rank structure. From another perspective, the anisotropic SSTV is globally imposed to reconstruct the low-rank patches of the image and effectively preserve both the spatial and spectral smoothness of the whole HSI. With this strategy, the small amount of noise in the local low-rank patches can be further removed, and the edge information of the reconstructed HSI is globally strengthened. In return, the globally reconstructed HSI feeds back to help the decomposition of the local low-rank clean components and the sparse noise. This procedure goes on alternately until convergence. The augmented Lagrange multiplier (ALM) method used in the proposed LLRSSTV model is presented in the following part.

C. Optimization Procedure

To efficiently solve the proposed LLRSSTV model (8), we first introduce three auxiliary variables $\mathcal{J},\ \mathcal{X} \in \mathbb{R}^{M\times N\times p}$, and

$\mathcal{U} \in \mathbb{R}^{M\times N\times p\times 3}$, and we obtain the following formulation:

$$\begin{aligned} &\min_{\mathcal{L},\mathcal{S},\mathcal{J},\mathcal{X},\mathcal{U}} \sum_{i,j} (||\mathcal{L}_{i,j}||_* + \lambda||\mathcal{S}_{i,j}||_1) + \tau||\mathcal{U}||_1 \\ &\text{s.t.,}\ \mathcal{L}_{i,j} = \mathcal{J}_{i,j}, \mathcal{J} = \mathcal{X},\ \mathcal{U} = \mathbf{D}\mathcal{X}, \\ &||\mathcal{O}_{i,j} - \mathcal{L}_{i,j} - \mathcal{S}_{i,j}||_F^2 \le \varepsilon,\ \text{rank}\ (\mathcal{L}_{i,j}) \le r \end{aligned} \tag{9}$$

in which $\mathbf{D} = [\tau_i\mathbf{D}_i, \tau_j\mathbf{D}_j, \tau_b\mathbf{D}_b]$ denotes the TV operator in the spatial and spectral directions. This problem can be efficiently solved by the ALM method, which minimizes the following augmented Lagrangian function:

$$\begin{aligned} \min \ell\,(\mathcal{L},\mathcal{S},\mathcal{J},\mathcal{X},\mathcal{U}) = &\min_{\mathcal{L},\mathcal{S},\mathcal{J},\mathcal{X},\mathcal{U}} \sum_{i,j} (||\mathcal{L}_{i,j}||_* + \lambda||\mathcal{S}_{i,j}||_1 \\ &+ \left\langle \mathcal{Y}^{\mathcal{O}}_{i,j}, \mathcal{O}_{i,j} - \mathcal{L}_{i,j} - \mathcal{S}_{i,j} \right\rangle + \frac{\mu}{2}\,\|\mathcal{O}_{i,j} - \mathcal{L}_{i,j} - \mathcal{S}_{i,j}\|_F^2 \\ &+ \left\langle \mathcal{Y}^{\mathcal{L}}_{i,j}, \mathcal{L}_{i,j} - \mathcal{J}_{i,j} \right\rangle + \frac{\mu}{2}\,\|\mathcal{L}_{i,j} - \mathcal{J}_{i,j}\|_F^2 \Big) + \tau||\mathcal{U}||_1 \\ &+ \langle \mathcal{Y}, \mathcal{U} - \mathbf{D}\mathcal{X} \rangle + \langle \mathcal{Y}^{x}, \mathcal{J} - \mathcal{X} \rangle \\ &+ \frac{\mu}{2}\left(\|\mathcal{U} - \mathbf{D}\mathcal{X}\|_2^2 + \|\mathcal{J} - \mathcal{X}\|_2^2\right) \\ \text{s.t.,}\ \text{rank}\ (\mathcal{L}_{i,j}) \le r & \end{aligned} \tag{10}$$

where μ is the penalty parameter, and $\mathcal{Y}^{\mathcal{O}}_{i,j}$, $\mathcal{Y}^{\mathcal{L}}_{i,j}$, $\mathcal{Y}$, and $\mathcal{Y}^{x}$ are the Lagrangian multipliers. In addition, $\mathcal{Y} = [\mathcal{Y}_1, \mathcal{Y}_2, \mathcal{Y}_3]$, $\mathcal{U} = [\mathcal{U}_1, \mathcal{U}_2, \mathcal{U}_3]$, and the norm $\|\cdot\|_2^2$ stands for the sum of squares of all the elements for both the 3-model and 4-model tensors.

Typically, a natural way to solve this problem is to iteratively optimize the augmented Lagrangian function (10) over one variable while fixing the others. We categorize the update in the $k+1$th iteration as two problems:

$$(\mathcal{L}^{k+1}, \mathcal{S}^{k+1}) = \arg\min_{\mathcal{S},\mathcal{L}} \ell\,(\mathcal{L}, \mathcal{S}, \mathcal{J}^{k}),\ \text{s.t.,}\ \text{rank}\ (\mathcal{L}_{i,j}) \le r \tag{11a}$$

$$(\mathcal{J}^{k+1}, \mathcal{X}^{k+1}, \mathcal{U}^{k+1}) = \arg\min_{\mathcal{J},\mathcal{X},\mathcal{U}} \ell\,(\mathcal{L}^{k+1}_{i,j}, \mathcal{J}, \mathcal{X}, \mathcal{U}) \tag{11b}$$

where (11a) can be regarded as the local patch-wise low-rank and sparse matrix decomposition problem; meanwhile, (11b) is the SSTV-regularized global image reconstruction problem from these denoised low-rank patches.

1) *Local low-rank and sparse matrix decomposition optimization for*$(\mathcal{L}, \mathcal{S})$*:* with the other parameters fixed, the subproblem for $(\mathcal{L}, \mathcal{S})$ simplifies to

$$\begin{aligned} \arg\min_{\mathcal{L},\mathcal{S}} &\sum\nolimits_{i,j} (||\mathcal{L}_{i,j}||_* + \lambda||\mathcal{S}_{i,j}||_1 \\ &+ \left\langle \mathcal{Y}^{\mathcal{O}}_{i,j}, \mathcal{O}_{i,j} - \mathcal{L}_{i,j} - \mathcal{S}_{i,j} \right\rangle \\ &+ \frac{\mu}{2}\,\|\mathcal{O}_{i,j} - \mathcal{L}_{i,j} - \mathcal{S}_{i,j}\|_F^2 + \left\langle \mathcal{Y}^{\mathcal{L}}_{i,j}, \mathcal{L}_{i,j} - \mathcal{J}_{i,j} \right\rangle \\ &+ \frac{\mu}{2}\,\|\mathcal{L}_{i,j} - \mathcal{J}_{i,j}\|_F^2 \Big) \\ \text{s.t.,}\ &\text{rank}\ (\mathcal{L}_{i,j}) \le r. \end{aligned} \tag{12}$$

To solve the problem (12), we adopt the idea proposed in [46] and perform rank-constrained RPCA on a family of patches $\{\mathcal{O}_{i,j}\}$, accumulating a weighted sum of the results $\{\mathcal{L}_{i,j}, \mathcal{S}_{i,j}\}$ to reconstruct $(\mathcal{L}, \mathcal{S})$. The optimization for each $(\mathcal{L}_{i,j}, \mathcal{S}_{i,j})$ pair can be reformulated as

$$\begin{aligned} \arg\min_{\mathcal{L}_{i,j}, \mathcal{S}_{i,j}} &\|\mathcal{L}_{i,j}\|_* + \lambda\|\mathcal{S}_{i,j}\|_1 + \left\langle \mathcal{Y}^{\mathcal{O}}_{i,j}, \mathcal{O}_{i,j} - \mathcal{L}_{i,j} - \mathcal{S}_{i,j} \right\rangle \\ &+ \frac{\mu}{2}\,\|\mathcal{O}_{i,j} - \mathcal{L}_{i,j} - \mathcal{S}_{i,j}\|_F^2 + \left\langle \mathcal{Y}^{\mathcal{L}}_{i,j}, \mathcal{L}_{i,j} - \mathcal{J}_{i,j} \right\rangle \\ &+ \frac{\mu}{2}\,\|\mathcal{L}_{i,j} - \mathcal{J}_{i,j}\|_F^2\ \text{s.t.,}\ \text{rank}\ (\mathcal{L}_{i,j}) \le r. \end{aligned} \tag{13}$$

We alternately update the two variables with the following strategy, and the optimization of (13) is reduced to two simpler minimization subproblems.

a) The $\mathcal{L}_{i,j}$-related subproblem is

$$\begin{aligned} &\arg\min_{\text{rank}\ (\mathcal{L}_{i,j}) \le r} ||\mathcal{L}_{i,j}||_* + \frac{\mu}{2}\left\|\mathcal{O}_{i,j} - \mathcal{L}_{i,j} - \mathcal{S}_{i,j} + \mathcal{Y}^{\mathcal{O}}_{i,j}/\mu\right\|_F^2 \\ &\quad + \frac{\mu}{2}\left\|\mathcal{L}_{i,j} - \mathcal{J}_{i,j} + \mathcal{Y}^{\mathcal{L}}_{i,j}/\mu\right\|_F^2 \\ &= \arg\min_{\text{rank}\ (\mathcal{L}_{i,j}) \le r} ||\mathcal{L}_{i,j}||_* + \frac{1}{2} \times 2\mu \\ &\quad \times \Big\|\mathcal{L}_{i,j} - ((\mathcal{O}_{i,j} - \mathcal{S}_{i,j} + \mathcal{J}_{i,j})/2 \\ &\quad + (\mathcal{Y}^{\mathcal{O}}_{i,j} - \mathcal{Y}^{\mathcal{L}}_{i,j})/(2\mu)\Big)\Big\|_F^2. \end{aligned} \tag{14}$$

The step for updating $\mathcal{L}$ can be solved by the following Lemma 1.

Lemma 1: [49]. We let $\mathbf{W} \in \mathbb{R}^{mn\times p}$ be a given matrix, where the singular value decomposition (SVD) of matrix $\mathbf{W}$ of rank r is defined as

$$\mathbf{W} = U\mathrm{E_r}V^*, \quad \mathrm{E_r} = \text{diag}\ (\{\sigma_i\}_{1\le i\le r}).$$

The singular value shrinkage operator then obeys

$$D_\delta(\mathbf{W}) = \arg\min_{\text{rank}\ (\mathbf{L}) \le r} \delta||\mathbf{L}||_* + \frac{1}{2}||\mathbf{L} - \mathbf{W}||_F^2$$

where $D_\delta(\mathbf{W}) = UD_\delta(\mathrm{E_r})V^*$, $D_\delta(\mathrm{E_r}) = \text{diag}\ \{\max\ ((\sigma_i - \delta), 0)\}$.

By using Lemma 1, we can immediately obtain the optimization result for (14):

$$\mathcal{L}_{i,j} = D_{1/(2\mu)}\Big((\mathcal{O}_{i,j} - \mathcal{S}_{i,j} + \mathcal{J}_{i,j})/2 + (\mathcal{Y}^{\mathcal{O}}_{i,j} - \mathcal{Y}^{\mathcal{L}}_{i,j})/(2\mu)\Big). \tag{15}$$

b) The $\mathbf{S}_{i,j}$-related subproblem is

$$\begin{aligned} &\arg\min_{\mathcal{S}_{i,j}} \lambda||\mathcal{S}_{i,j}||_1 + \frac{\mu}{2}\left\|\mathcal{O}_{i,j} - \mathcal{L}_{i,j} - \mathcal{S}_{i,j} + \mathcal{Y}^{\mathcal{O}}_{i,j}/\mu\right\|_F^2 \\ &= \Re_{\lambda/\mu}(\mathcal{O}_{i,j} - \mathcal{L}_{i,j} + \mathcal{Y}^{\mathcal{O}}_{i,j}/\mu) \end{aligned} \tag{16}$$

where $\Re_{\lambda/\mu}(\cdot)$ is the soft-thresholding (shrinkage) operator defined as follows [50]:

$$\Re_{\lambda/\mu}(x) = \begin{cases} x - \lambda/\mu, & \text{if } x > \lambda/\mu \\ x + \lambda/\mu, & \text{if } x < -\lambda/\mu \\ 0, & \text{otherwise} \end{cases}.$$

2) *Global SSTV-regularized image reconstruction optimization for* $(\mathcal{J},\mathcal{X},\mathcal{U})$*:* Given $\{\mathcal{L}_{i,j}\}$ patches and the Lagrangian multipliers, the problem over $(\mathcal{J},\mathcal{X},\mathcal{U})$ is obtained as

$$\begin{aligned} \arg\min \ell\left(\mathcal{J},\mathcal{X},\mathcal{U}\right) = \min_{\mathcal{J},\mathcal{X},\mathcal{U}} \sum_{i,j} \Big(\left\langle \mathcal{Y}^{\mathcal{L}}_{i,j}, \mathcal{L}_{i,j} - \mathcal{J}_{i,j} \right\rangle \\ + \frac{\mu}{2}\left\|\mathcal{L}_{i,j} - \mathcal{J}_{i,j}\right\|_F^2 \Big) + \tau\|\mathcal{U}\|_1 + \langle \mathcal{Y}, \mathcal{U} - \mathbf{D}\mathcal{X} \rangle \\ + \left\langle \mathcal{Y}^{\mathcal{X}}, \mathcal{J} - \mathcal{X} \right\rangle + \frac{\mu}{2}\left(\|\mathcal{U} - \mathbf{D}\mathcal{X}\|_2^2 + \|\mathcal{J} - \mathcal{X}\|_2^2 \right). \end{aligned} \tag{17}$$

Analogously, we alternately update one variable while fixing the other two, and the update of $(\mathcal{J},\mathcal{X},\mathcal{U})$ in (17) is split into the following three subproblems.

a) The $\mathcal{J}$-related subproblem can be reformulated as

$$\begin{aligned} \arg\min_{\mathcal{J}} \frac{\mu}{2}\left\|\mathcal{J} - \mathcal{X} + \mathcal{Y}^{\mathcal{X}}/\mu\right\|_2^2 \\ + \sum\nolimits_{i,j} \left(\frac{\mu}{2}\left\|\mathcal{L}_{i,j} - \mathcal{J}_{i,j} + \mathcal{Y}^{\mathcal{L}}_{i,j}/\mu\right\|_F^2 \right). \end{aligned} \tag{18}$$

This is a convex function, which has the following closed-form solution:

$$\begin{aligned} \mathcal{J} = \left(\mathcal{X} - \mathcal{Y}^{\mathcal{X}}/\mu + \sum\nolimits_{i,j} R_{i,j}^T (\mathcal{L}_{i,j} + \mathcal{Y}^{\mathcal{L}}_{i,j}/\mu) \right) \\ ./\left(\mathbf{1} + \sum\nolimits_{i,j} R_{i,j}^T R_{i,j} \right) \end{aligned} \tag{19}$$

where the $R_{i,j}$ binary operator is defined before, $R_{i,j}^T$ is its inverse, and $\mathbf{1}$ stands for an all-one tensor of size $M \times N \times p$.

b) The $\mathcal{X}$-related subproblem can be given as

$$\arg\min_{\mathcal{X}} \frac{\mu}{2}\|\mathcal{U} - \mathbf{D}\mathcal{X} + \mathcal{Y}/\mu\|_2^2 + \frac{\mu}{2}\left\|\mathcal{J} - \mathcal{X} + \mathcal{Y}^{\mathcal{X}}/\mu\right\|_2^2. \tag{20}$$

It can be solved by considering the following normal equation:

$$(\mathbf{D}^T\mathbf{D} + \mathbf{1})\mathcal{X} = \mathbf{D}^T(\mathcal{U} + \mathcal{Y}/\mu) + (\mathcal{J} + \mathcal{Y}^{\mathcal{X}}/\mu) \tag{21}$$

which can be efficiently solved by the fast Fourier transform (FFT) method:

$$\mathbf{X} = \mathcal{F}^{-1}\left[\frac{\mathcal{F}\left((\mathbf{J} + \mathcal{Y}^{\mathcal{X}}/\mu) + \mathbf{D}^T(\mathbf{U} + \mathcal{Y}/\mu) \right)}{1 + (\mathcal{F}(\tau_i\mathbf{D}_i))^2 + (\mathcal{F}(\tau_j\mathbf{D}_j))^2 + (\mathcal{F}(\tau_b\mathbf{D}_b))^2} \right]. \tag{22}$$

In (22), $\mathcal{F}(\cdot)$ denotes the FFT, and $\mathcal{F}^{-1}$ is the inverse transform. $\mathbf{D}^T$ represents the adjoint operator of $\mathbf{D}$.

Algorithm 1: HSI denoising with the LLRSSTV algorithm.

```
Input: $M \times N \times p$ observed HSI $\mathcal{O}$, desired rank $r$, patch size $m \times n$, stopping criterion $\varepsilon$, regularization parameters $\lambda$, $\tau$, and $\tau_b$
Output: Denoised image $\mathcal{X}$
Initialize: $\mathcal{L} = \mathcal{X} = \mathcal{S} = \mathcal{J} = 0, \mathcal{U} = 0$, $\mathcal{Y}^{\mathcal{O}}_{i,j}, \mathcal{Y}^{\mathcal{L}}_{i,j}, \mathcal{Y}, \mathcal{Y}^{\mathcal{X}} = 0$, $\mu = 10^{-2}$, $\mu_{\max} = 10^6$, $\rho = 1.5$, and $k = 0$
Repeat until convergence
  · Local low-rank and sparse matrix decomposition via (11a)
  Update all $(\mathcal{L}_{i,j}, \mathcal{S}_{i,j})$ patches using (15) and (16), respectively
  · Global SSTV-regularized image reconstruction via (11b)
  Update $(\mathcal{J},\mathcal{X},\mathcal{U})$ using (19), (22), and (24), respectively
  · Update the Lagrangian multipliers using (25), and the penalty parameter update $\mu := \min(\rho\mu, \mu_{\max})$
  Check the convergence conditions:
    $\max\{||\mathcal{O}_{i,j} - \mathcal{L}^{k+1}_{i,j} - \mathcal{S}^{k+1}_{i,j}||_\infty, ||\mathcal{J}^{k+1} - \mathcal{X}^{k+1}||_\infty, ||\mathcal{U}^{k+1} - \mathbf{D}\mathcal{X}^{k+1}||_\infty\} \le \varepsilon.$
```

c) The $\mathcal{U}$-related subproblem has the following formulation:

$$\begin{aligned} &\arg\min_{\mathcal{U}} \tau||\mathcal{U}||_1 + \langle \mathcal{Y}, \mathcal{U} - \mathbf{D}\mathcal{X} \rangle + \frac{\mu}{2}\|\mathcal{U} - \mathbf{D}\mathcal{X}\|_2^2 \\ &= \arg\min_{\mathcal{U}} \tau||\mathcal{U}||_1 + \frac{\mu}{2}\|\mathcal{U} - \mathbf{D}\mathcal{X} + \mathcal{Y}/\mu\|_2^2 \end{aligned} \tag{23}$$

where $\mathcal{Y} = [\mathcal{Y}_1, \mathcal{Y}_2, \mathcal{Y}_3]$ and $\mathcal{U} = [\mathcal{U}_1, \mathcal{U}_2, \mathcal{U}_3]$. Likewise, the optimization (23) can be solved by the soft-thresholding (shrinkage) operator [the same as that of (16)]:

$$\begin{cases} \mathcal{U}_1 = \Re_{\tau/\mu}(\tau_i\mathbf{D}_i\mathcal{X} - \mathcal{Y}_1/\mu) \\ \mathcal{U}_2 = \Re_{\tau/\mu}(\tau_j\mathbf{D}_j\mathcal{X} - \mathcal{Y}_2/\mu) \\ \mathcal{U}_3 = \Re_{\tau/\mu}(\tau_b\mathbf{D}_b\mathcal{X} - \mathcal{Y}_3/\mu) \end{cases}. \tag{24}$$

After solving the two problems (11a) and (11b), the Lagrangian multipliers $\mathcal{Y}^{\mathcal{O}}_{i,j}$, $\mathcal{Y}^{\mathcal{L}}_{i,j}$, $\mathcal{Y}$, and $\mathcal{Y}^x$ can be updated in parallel as

$$\begin{cases} \mathcal{Y}^{\mathcal{O}}_{i,j} = \mathcal{Y}^{\mathcal{O}}_{i,j} + \mu(\mathcal{O}_{i,j} - \mathcal{L}_{i,j} - \mathcal{S}_{i,j}) \\ \mathcal{Y}^{\mathcal{L}}_{i,j} = \mathcal{Y}^{\mathcal{L}}_{i,j} + \mu(\mathcal{L}_{i,j} - \mathcal{J}_{i,j}) \\ \mathcal{Y} = \mathcal{Y} + \mu(\mathcal{U} - \mathbf{D}\mathcal{X}) \\ \mathcal{Y}^{\mathcal{X}} = \mathcal{Y}^{\mathcal{X}} + \mu(\mathcal{J} - \mathcal{X}) \end{cases}. \tag{25}$$

Summarizing the aforementioned description, we arrive at an augmented Lagrangian alternating direction procedure to solve the proposed LLRSSTV model, as presented in Algorithm 1.

In Algorithm 1, the inputs are the noisy HSI $\mathcal{O}$, the desired upper bound rank r, the patch size $m \times n$, the regularization parameters λ, τ, and τ_b, and the stopping criterion ε. ρ is the parameter introduced in the ADMM [44], which can be set as a constant value. The upper bound rank r represents the dimension of the HSI subspace. In [41], Peng *et al.* tried to estimate the rank of each patch by the use of the Akaike information criterion/minimum description length method. In our HSI degradation model, the image is assumed to be corrupted by mixed noise. As an alternative, we propose a simple way to estimate the upper bound rank r as follows. First, we use a median filter as a preprocessing step for the observed HSI to remove the sparse noise. Subsequently, a multiple regression theory based approach [51] is adopted to estimate the noise of the HSI. We then obtain the clean image $\mathbf{L}$ and the noise $\mathbf{N}$, which are the Casorati matrices of the clean HSI $\mathcal{O}$ and the noise $\mathcal{N}$, respectively. The singular values of $\mathbf{L}$ and $\mathbf{N}$ are denoted as $[\sigma_1, \ldots, \sigma_p]$, $[S_1, \ldots, S_p]$, respectively. We calculate the upper bound rank r as a natural number such that $\sigma_r \geq S_1$ and $\sigma_{r+1} < S_1$.

The patch size $m \times n$ is set to 20×20. The step size of the patch is 10×10 (i.e., we only use patches every ten pixels along both the horizontal and vertical directions), to speed up the computation. Parameter λ is the tradeoff between the local low-rank clean image and the sparse noise, and the regularization parameter τ is used to control the tradeoff between the nuclear norm and the SSTV norm. The analysis of parameters λ, τ, and τ_b is provided in the experimental part. Finally, the stopping criterion ε is set to 1e – 6.

We initialize $\mathcal{L} = \mathcal{X} = \mathcal{S} = \mathcal{J} = 0$, $\mathcal{U} = 0$, and also all the Lagrangian multipliers to be 0. For variable μ shown in the augmented Lagrangian function (10), we initialize it as 10^{-2} and update it as $\mu := \min\,(\rho\mu, \mu_{\max})$ in each iteration step. This strategy of determining the variable μ has been widely used in the ALM-based methods, and it can support the convergence of the algorithm [50]. Finally, the output of Algorithm 1 is the denoised image $\mathcal{X} \in \mathbb{R}^{M \times N \times p}$.

IV. EXPERIMENTAL RESULTS AND DISCUSSION

Both simulated and real data experiments were undertaken to demonstrate the effectiveness of the proposed LLRSSTV method for HSI denoising. We selected eight different noise removal methods for comparison, i.e., SSAHTV [23], SSTV [25], the block-matching and four-dimensional filtering algorithm (BM4D) [52], low-rank representation with spectral difference space (LRRSDS) [48], noise-adjusted iterative low-rank matrix approximation (NAILRMA) [15], fast hyperspectral image denoising based on low-rank and sparse representations (FastHyDe)[1] [24], low-rank constraint and SSTV (LSSTV) [37], low-rank matrix recovery (LRMR) [14], and the TV-regularized low-rank method (LRTV) [35]. However, it should be noted that the SSAHTV, SSTV, BM4D, NAILRMA, and FastHyDe methods are only suitable for the case of Gaussian noise and slight sparse noise. Before the denoising, the gray values of each HSI band were normalized to [0, 1]. For SSAHTV and SSTV, the regularization parameters were manually adjusted to the optimal in each experiment to balance the fidelity term and the TV regularization term. BM4D and NAILRMA are parameter-free methods. For LRRSDS, FastHyDe, LSSTV, LRMR, and LRTV, the parameter selection was consistent with the description in the original papers.

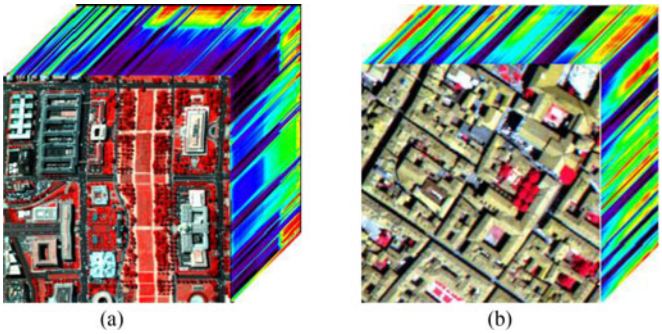
Fig. 3. (a) HYDICE Washington DC Mall dataset used in the simulated experiment (R: 60, G: 27, B: 17). (b) Pavia city center dataset used in the simulated experiment (R: 80, G: 34, B: 9).

A. *Simulated HSI Data Experiments*

1) Data Description: In the simulated data experiments, two HSI datasets were adopted. The first dataset was the Washington DC Mall dataset,[2] which was collected by the hyperspectral digital imagery collection experiment (HYDICE) sensor [48]. The whole image contains 1208 × 307 pixels and 191 spectral bands. In the experiments, a subimage of size 256 × 256 × 191 was used, which is presented in Fig. 3(a). The Pavia city center dataset[3] was collected by the reflective optics system imaging spectrometer (ROSIS-03). As some spectral bands of the Pavia city center dataset are heavily contaminated by noise, they cannot be used as the reference for denoising. Therefore, the first few bands of this data were removed, and the size of the subimage was selected as 200 × 200 × 80, which is shown in Fig. 3(b). For the simulated experiments, we used the peak SNR (PSNR) index, the structural similarity index (SSIM) [53], and the mean spectral angle distance (MSAD) to give a quantitative assessment of the results achieved by the different methods. For the HSI, we computed the PSNR and SSIM values between each noise-free band and denoised band, and then averaged them. These metrics are denoted as mean PSNR (MPSNR) and mean SSIM index (MSSIM). The MSAD is defined as

$$\mathrm{MSAD} = \frac{1}{MN} \sum_{i=1}^{MN} \frac{180}{\pi} \times \arccos \frac{(\mathcal{X}^i)^T \cdot (\hat{\mathcal{X}}^i)}{||\mathcal{X}^i|| \cdot ||\hat{\mathcal{X}}^i||} \tag{26}$$

where $\mathcal{X}^i$ and $\hat{\mathcal{X}}^i$ are the ith spectral signatures of the noise-free and denoised HSIs, respectively.

To simulate a noisy image, we added Gaussian noise, salt-and-pepper impulse noise, and stripes to all the bands of the two HSI datasets, as in the following four cases.

---

[1] The MATLAB code was provided by Dr. Lina Zhuang, and the extension of the conference paper has been submitted to IEEE JOURNAL OF SELECTED TOPICS IN APPLIED EARTH OBSERVATIONS AND REMOTE SENSING.

[2] Available: https://engineering.purdue.edu/~biehl/MultiSpec/hyperspectral.html

[3] Available: http://www.ehu.es/ccwintco/index.php/Hyperspectral_Remote_Sensing_Scenes

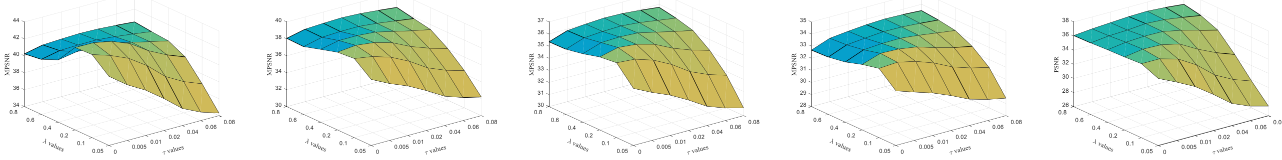

(a) (b) (c) (d) (e)

Fig. 4. MPSNR values of LLRSSTV on the Washington DC Mall image, as related to parameters λ and τ. The data were corrupted by the noise simulated in case 1 with (a) $G = 0.025$ and $P = 0.05$, (b) $G = 0.05$ and $P = 0.1$, (c) $G = 0.075$ and $P = 0.15$, (d) $G = 0.1$ and $P = 0.2$, and (e) in case 3.

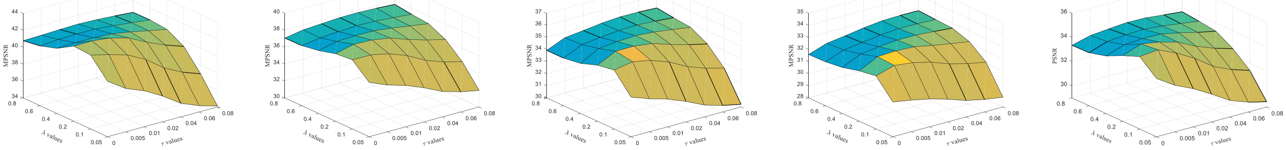

(a) (b) (c) (d) (e)

Fig. 5. MPSNR values of LLRSSTV on the Pavia city center image, as related to parameters λ and τ. The data were corrupted by the noise simulated in case 1 with (a) $G = 0.025$ and $P = 0.05$, (b) $G = 0.05$ and $P = 0.1$, (c) $G = 0.075$ and $P = 0.15$, (d) $G = 0.1$ and $P = 0.2$, and (e) in case 3.

Case 1: Zero-mean Gaussian noise was added to all the bands of the Washington DC Mall and Pavia city center data. The variances of the Gaussian noise were $G = 0.025$, 0.05, 0.075, and 0.1. Meanwhile, the impulse noise was also added to all the bands to simulate sparse noise. The percentages of the impulse noise were $P = 0.05$, 0.1, 0.15, and 0.2, correspondingly.

Case 2: For this case, the noise intensity was different for the different bands. Different-intensity noise was added to each band, with the variance of the Gaussian noise being randomly selected from 0 to 0.2.

Case 3: On the basis of case 2, impulse noise was added to all the bands. The impulse noise intensity of the different bands was different, with the percentage being randomly selected from 0 to 0.2.

Case 4: On the basis of case 3, 30% of the bands were randomly selected to have stripes added [5]. The stripe number of each selected band was randomly selected from 3 to 15.

2) Parameter Analysis: In the proposed LLRSSTV method, the choice of the regularization parameters λ and τ, the upper bound rank r, the patch size $m \times n$, and parameter τ_b determines the HSI denoising results. Next, we discuss the influence of these parameters on the LLRSSTV denoising.

We first present the influence of parameters λ and τ on the denoising results of the two HSI datasets corrupted by simulated noise in case 1. Notably, we fixed the patch size as $m \times n = 20 \times 20$ and parameters $(\tau_i, \tau_j, \tau_b) = (1, 1, 0.5)$, as recommended in [25]. The upper bound rank r was estimated by the method described in Section III-C. The proposed LLRSSTV was then tested using different values of parameters λ and τ, with λ varied between 0.05, 0.1, 0.2, 0.4, 0.6, and 0.8 and τ varied between 0, 0.005, 0.01, 0.02, 0.04, 0.06, and 0.08. When $\tau = 0$, the proposed LLRSSTV method reduces to the local low-rank-based method with a traditional weighted average based patch reconstruction strategy [8] in each iteration step.

Figs. 4 and 5 report the MPSNR values of LLRSSTV on the two datasets, as related to parameters λ and τ. From Figs. 4(a) and 5(a), it can be observed that the performance of the proposed LLRSSTV is similar when τ is 0 and 0.005. That is to say, the TV-based image reconstruction performs the same as the traditional weighted average based method in the low-noise case. However, when the noise level increases, the advantage of the TV-based image reconstruction becomes apparent. As presented in Figs. 4(b)–(e) and 5(b)–(e), the MPSNR values in the case of $\tau = 0.005$ are higher than those of $\tau = 0$. From these figures, it is not easy to select the optimal values of parameters λ and τ for all the cases of noise level. Fortunately, the denoising results of LLRSSTV maintain robustness as λ and τ change. In the simulated and real data experiments, we fixed the parameters as $\lambda = 0.2$ and $\tau = 0.005$, which could ensure acceptable denoising results in all the noise levels.

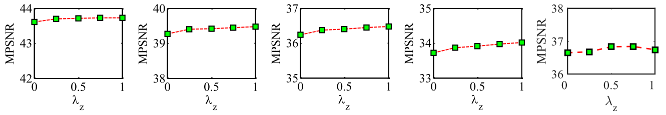

(a) (b) (c) (d) (e)

Fig. 6. MPSNR values of LLRSSTV on the Washington DC Mall image as parameter τ_b is changed. The data were corrupted by the noise simulated in case 1 with (a) $G = 0.025$ and $P = 0.05$, (b) $G = 0.05$ and $P = 0.1$, (c) $G = 0.075$ and $P = 7\ 0.15$, (d) $G = 0.1$ and $P = 0.2$, and (e) in case 3.

Subsequently, we investigated the effect of the spectral TV regularization by varying τ_b between 0, 0.25, 0.5, 0.75, and 1. Similarly, we fixed the parameters as $\lambda = 0.2$, $\tau = 0.005$, and $(\tau_i, \tau_j) = (1, 1)$. The upper bound rank r was estimated by the method described in Section III-C. When τ_b is set to 0, the SSTV-regularized image reconstruction method reduces to the band-by-band TV-regularized-based method. Fig. 6 shows the results obtained with the Washington DC Mall image, and Fig. 7 presents the results obtained with the Pavia city center image. It is clear that the denoised results when τ_b is larger than 0 are better than those when τ_b is equal to 0. This confirms the contribution of the spectral smoothness according to the spec-

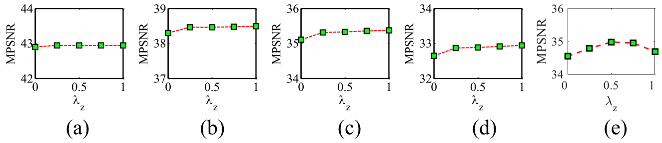

Fig. 7. MPSNR values of LLRSSTV on the Pavia city center image as parameter τ_b is changed. The data were corrupted by the noise simulated in case 1 with (a) $G = 0.025$ and $P = 0.05$, (b) $G = 0.05$ and $P = 0.1$, (c) $G = 0.075$ and $P = 7\ 0.15$, (d) $G = 0.1$ and $P = 0.2$, and (e) in case 3.

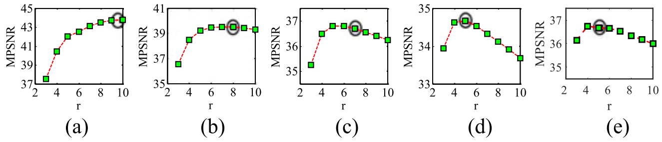

Fig. 8. MPSNR values of LLRSSTV on the Washington DC Mall image as the upper bound rank r parameter is changed. The data were corrupted by the noise simulated in case 1 with (a) $G = 0.025$ and $P = 0.05$, (b) $G = 0.05$ and $P = 0.1$, (c) $G = 0.075$ and $P = 0.15$, (d) $G = 0.1$ and $P = 0.2$, and (e) case 3.

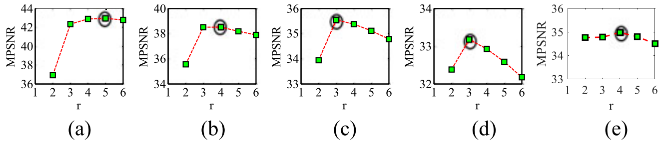

Fig. 9. MPSNR values of LLRSSTV on the Pavia city center image as the upper bound rank r parameter is changed. The data were corrupted by the noise simulated in case 1 with (a) $G = 0.025$ and $P = 0.05$, (b) $G = 0.05$ and $P = 0.1$, (c) $G = 0.075$ and $P = 0.15$, (d) $G = 0.1$ and $P = 0.2$, and (e) case 3.

tral consistency. Typically, the value of τ_b indicates the spectral consistency intensity of the HSI. In our experiments, we fixed parameter τ_b as 0.5, which achieves an acceptable denoising result. Furthermore, for other cases, we can decrease the τ_b value when the spectral consistency intensity of the HSI is low and increase the value otherwise.

The upper bound rank r represents the separation boundary of signal and noise. It means that, for each patch, the first r principal components of the patch are more likely to be the clean signal, and the rest of the principal components are noise. Figs. 8 and 9 show the analysis of the upper bound rank r of the proposed method with the two datasets by fixing the other parameters. As presented in the figures, for both datasets, the best value of the upper bound rank r is larger when the simulated noise level is lower, and the value is smaller otherwise. The reason for this is that when the noise level is higher, it is more difficult to discern the signal from the noise and, as a result, only a few signals can survive amongst the noise. The black oval marked in each figure represents the rank estimated by the proposed multiple regression theory based approach. It can be clearly observed that, in all cases, the estimated r provides the optimal or suboptimal evaluation values in terms of the MPSNR criterion.

We also analyzed the influence of the patch size, to validate the local low-rank property of the HSI. In the experiments, we set $m = n$ and changed them synchronously between 10, 20 40, 60, 80, and 256(200). Since, for different patch sizes, the optimal parameter pairs λ and τ are different, we selected them from [0.05, 0.1, 0.2, 0.4, 0.6, 0.8] and [0, 0.005, 0.01, 0.02, 0.04, 0.06, 0.08], respectively, to obtain the highest MPSNR values. Parameter τ_b was set as 0.5, the step size was $m/2 \times n/2$, and the upper bound rank r was estimated by the proposed method. Figs. 10 and 11 present the results of the proposed LLRSSTV on the two datasets with different patch sizes. Generally speaking, with the increase of the patch size, the MPSNR values obtained by LLRSSTV decrease. In particular, the MPSNR values obtained in the case of a patch size of 256 in the Washington DC Mall image and 200 in the Pavia city center image are much lower than those achieved when the patch size is 20. This demonstrates the efficiency of modeling the low-rank property of the HSI locally instead of globally. From another aspect, the highest MPSNR values are obtained by LLRSSTV with a patch size of 20 × 20, which inspired us to set the patch size in all the experiments as 20 × 20, to be consistent with the LRMR method in [14].

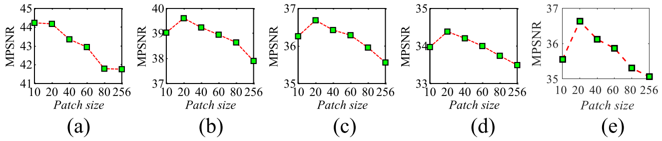

Fig. 10. MPSNR values of LLRSSTV on the Washington DC Mall image as the patch size $m \times n$ is changed. The data were corrupted by the noise simulated in case 1 with (a) $G = 0.025$ and $P = 0.05$, (b) $G = 0.05$ and $P = 0.1$, (c) $G = 0.075$ and $P = 0.15$, (d) $G = 0.1$ and $P = 0.2$, and (e) in case 3.

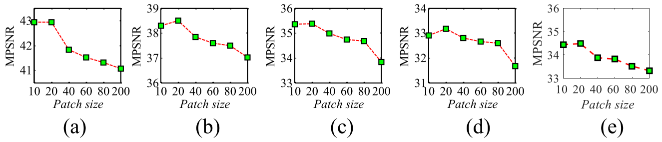

Fig. 11. MPSNR values of LLRSSTV on the Pavia city center image as the patch size $m \times n$ is changed. The data were corrupted by the noise simulated in case 1 with (a) $G = 0.025$ and $P = 0.05$, (b) $G = 0.05$ and $P = 0.1$, (c) $G = 0.075$ and $P = 0.15$, (d) $G = 0.1$ and $P = 0.2$, and (e) in case 3.

Up to this point, all the parameters in the proposed LLRSSTV can be fixed or adaptively selected. Parameters λ and τ were fixed as 0.2 and 0.005, the SSTV regularizations were set as $\tau_b = 0.5$, the patch size of each local patch was set as 20 × 20, and the upper bound rank r of all the patches was estimated by the utilized multiple regression theory based approach.

3) Comparison With Other Methods: In this section, we describe how we compared the proposed LLRSSTV method with other HSI denoising methods on simulated noisy data. Table I reports the quantitative evaluation results of the different denoising methods with the simulated noise in cases 1–4 for the Washington DC Mall image and the Pavia city center image. The best results for each quality index are labeled in bold, and the second-best results are underlined. On the whole, the proposed method achieves the highest MPSNR and MSSIM values in most cases when compared to the other methods, indicating the advantage of the proposed method in HSI denoising. The quantitative evaluation results for SSTV are better than those for SSAHTV, because of the role of the spectral smoothness regularization. LRMR divides the HSI into overlapping patches

TABLE I
QUANTITATIVE EVALUATION RESULTS OF THE DIFFERENT DENOISING METHODS WITH THE SIMULATED NOISE IN CASES 1–4 ON THE TWO HSI DATASETS

Data	Noise case	Level	Evaluation index	SSAHTV	SSTV	BM4D	LRRSDS	NAILRMA	FastHyDe	LSSTV	LRMR	LRTV	LLRSSTV
Washington DC Mall image	Case 1	$G = 0.025$ $P = 0.05$	MPSNR	25.13	27.12	26.23	39.31	31.51	38.85	42.28	42.40	41.17	**44.16**
			MSSIM	0.653	0.814	0.812	0.984	0.922	0.985	0.989	0.989	0.988	**0.992**
			MSAD	12.07	12.41	13.09	5.46	7.54	4.10	2.89	3.62	3.07	**2.88**
		$G = 0.05$ $P = 0.1$	MPSNR	22.55	24.32	23.48	35.83	26.79	29.11	38.34	36.94	37.50	**39.60**
			MSSIM	0.505	0.729	0.605	0.962	0.844	0.906	0.975	0.967	0.972	**0.980**
			MSAD	12.83	14.43	15.98	7.03	10.09	7.90	**4.02**	5.81	4.57	4.14
		$G = 0.075$ $P = 0.15$	MPSNR	20.77	22.39	23.39	32.99	23.49	24.02	35.81	32.71	35.17	**36.68**
			MSSIM	0.450	0.668	0.604	0.926	0.766	0.804	0.957	0.926	0.951	**0.964**
			MSAD	15.91	15.75	14.70	9.02	12.41	11.47	6.07	7.87	5.73	**5.23**
		$G = 0.1$ $P = 0.2$	MPSNR	19.21	20.22	21.71	30.73	21.20	21.52	33.32	29.24	33.18	**34.37**
			MSSIM	0.379	0.537	0.552	0.881	0.69	0.731	0.918	0.871	0.926	**0.946**
			MSAD	16.37	17.34	14.76	10.98	14.29	13.65	7.08	9.84	6.85	**6.04**
	Case 2	Gaussian	MPSNR	27.36	29.95	31.43	35.02	39.0	**40.79**	36.89	34.97	36.17	38.67
			MSSIM	0.736	0.852	0.868	0.951	0.979	**0.991**	0.961	0.955	0.958	0.981
			MSAD	11.22	10.38	11.79	7.89	5.09	**4.27**	5.23	7.13	5.89	5.03
	Case 3	Gaussian + impulse	MPSNR	21.99	23.66	24.14	34.32	25.79	31.64	35.75	33.70	34.39	**36.59**
			MSSIM	0.486	0.711	0.630	0.944	0.817	0.915	0.944	0.941	0.938	**0.968**
			MSAD	14.90	14.73	16.37	8.11	12.33	13.07	7.42	7.50	8.21	**5.90**
	Case 4	Gaussian +stripes+ impulse	MPSNR	22.15	23.05	24.10	34.12	25.13	30.95	35.52	33.20	33.44	**36.27**
			MSSIM	0.513	0.615	0.628	0.942	0.803	0.908	0.939	0.935	0.928	**0.972**
			MSAD	16.35	16.13	16.35	8.27	12.69	13.34	8.37	7.64	8.16	**5.93**
Pavia city center image	Case 1	$G = 0.025$ $P = 0.05$	MPSNR	25.60	28.20	27.15	42.17	31.06	**43.53**	40.48	41.09	40.43	42.99
			MSSIM	0.696	0.837	0.805	0.989	0.914	**0.993**	0.987	0.989	0.985	0.991
			MSAD	10.12	9.23	8.46	3.12	6.099	**2.539**	3.184	3.15	3.30	2.98
		$G = 0.05$ $P = 0.1$	MPSNR	23.95	25.31	25.2	36.93	28.84	35.09	36.82	35.89	36.48	**38.29**
			MSSIM	0.592	0.757	0.701	0.962	0.883	0.970	0.969	0.960	0.963	**0.974**
			MSAD	10.62	10.38	10.37	5.37	7.12	**4.05**	4.74	5.31	4.98	4.50
		$G = 0.075$ $P = 0.15$	MPSNR	21.52	23.15	24.30	32.75	24.92	25.60	34.41	31.88	33.95	**35.33**
			MSSIM	0.502	0.692	0.682	0.910	0.821	0.853	0.947	0.913	0.936	**0.954**
			MSAD	13.85	10.86	9.24	8.06	8.37	7.27	5.49	7.08	6.42	**5.17**
		$G = 0.1$ $P = 0.2$	MPSNR	20.04	21.29	22.47	30.12	21.78	22.29	32.37	29.00	31.58	**33.13**
			MSSIM	0.459	0.621	0.617	0.853	0.702	0.771	0.919	0.861	0.898	**0.928**
			MSAD	12.68	11.70	9.83	9.96	9.20	8.37	6.18	8.14	7.89	**5.82**
	Case 2	Gaussian	MPSNR	27.64	30.31	32.00	35.86	37.93	**39.25**	36.21	34.98	35.96	36.86
			MSSIM	0.7576	0.873	0.894	0.946	0.974	0.982	0.958	0.954	0.948	**0.987**
			MSAD	14.43	7.81	10.16	6.78	4.57	**3.91**	4.78	6.60	8.96	5.12
	Case 3	Gaussian + impulse	MPSNR	22.41	24.43	25.31	34.10	28.41	31.55	34.46	32.58	33.67	**34.98**
			MSSIM	0.551	0.768	0.710	0.922	0.872	0.922	0.941	0.924	0.931	**0.956**
			MSAD	14.50	10.98	10.89	7.27	7.33	7.04	**4.95**	6.88	7.07	5.87
	Case 4	Gaussian +stripes+ impulse	MPSNR	22.35	23.71	25.14	33.90	25.38	32.63	34.33	32.12	33.31	**34.47**
			MSSIM	0.547	0.666	0.701	0.921	0.811	0.945	0.941	0.920	0.928	**0.952**
			MSAD	14.81	12.42	11.29	7.37	9.33	8.21	**6.03**	6.85	7.95	6.64

and processes each patch individually with the weighted average based patch reconstruction. In contrast, in the proposed LLRSSTV method, all the patches are processed together and the SSTV-regularized method is adopted to reconstruct the whole 3-D HSI. As a result, the improvement of LLRSSTV compared to LRMR demonstrates the contribution of the SSTV-regularized image reconstruction, which is a major contribution of the proposed method. LRRSDS and LSSTV achieve relatively good denoising results, but the quantitative evaluation results achieved by these two methods are still poorer than those of LLRSSTV. NAILRMA and FastHyDe appear suitable for the case of Gaussian noise removal. However, when the sparse noise intensity increases, the performance of the NAILRMA and FastHyDe methods decreases sharply. LRTV models the low-rank property of the HSI globally, combined with a spatial band-by-band TV regularization, which can be regarded as a special case of LLRSSTV. Compared to LRTV, the better quantitative evaluation results for LLRSSTV indicate the superiority of modeling the low-rank property of the HSI locally, along with the spectral smoothness regularization.

Fig. 12 shows the results of the different denoising methods with the Washington DC Mall image in case 3. Fig. 12(a) presents the false-color composite of the Washington DC Mall image. The image was contaminated by the mixed noise simulated in case 3, as presented in Fig. 12(b). Fig. 12(c)–(l) displays the denoising results of the different methods. The average

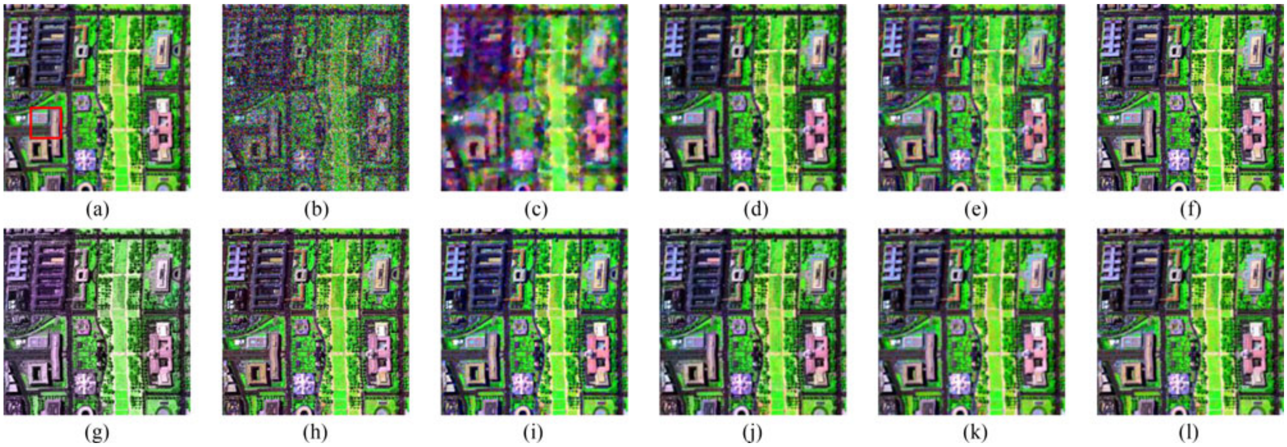

Fig. 12. Washington DC Mall image before and after denoising. The PSNR values are averaged with the three presented bands. (a) Original false-color image (R: 145, G: 68, B: 17). (b) Noisy image with the simulated noise in case 3 (11.55 dB). The image denoising results of (c) SSAHTV (19.55 dB), (d) SSTV (23.71 dB), (e) BM4D (22.83 dB), (f) LRRSDS (34.91 dB), (g) NAILRMA (23.76 dB), (h) FastHyDe (25.68 dB), (i) LSSTV (33.43 dB), (j) LRMR (31.95 dB), (k) LRTV (32.29 dB), and (l) LLRSSTV (36.06 dB).

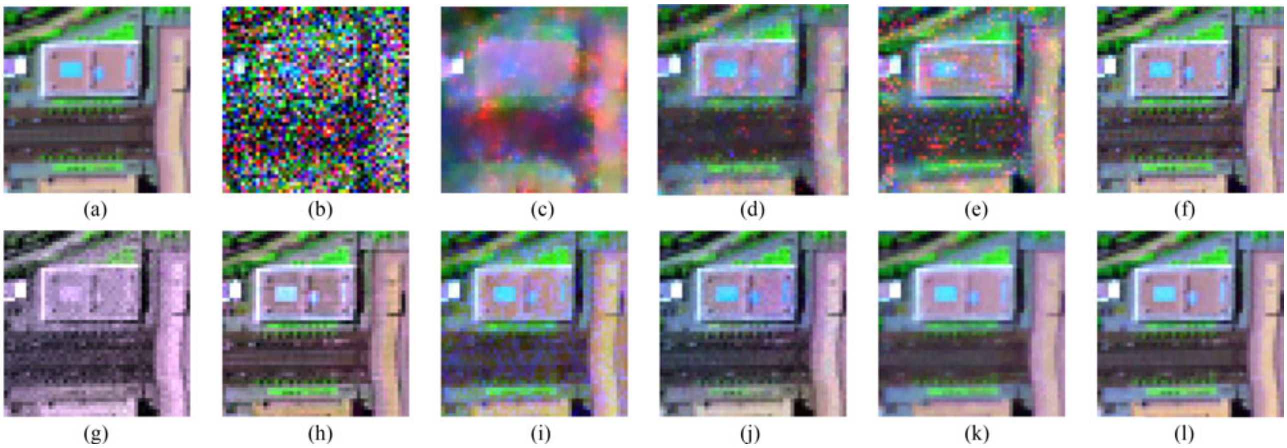

Fig. 13. Magnified results of Fig. 12. (a) Original band. (b) Noisy image. The image denoising results of (c) SSAHTV, (d) SSTV, (e) BM4D, (f) LRRSDS, (g) NAILRMA, (h) FastHyDe, (i) LSSTV, (j) LRMR, (k) LRTV, and (l) LLRSSTV.

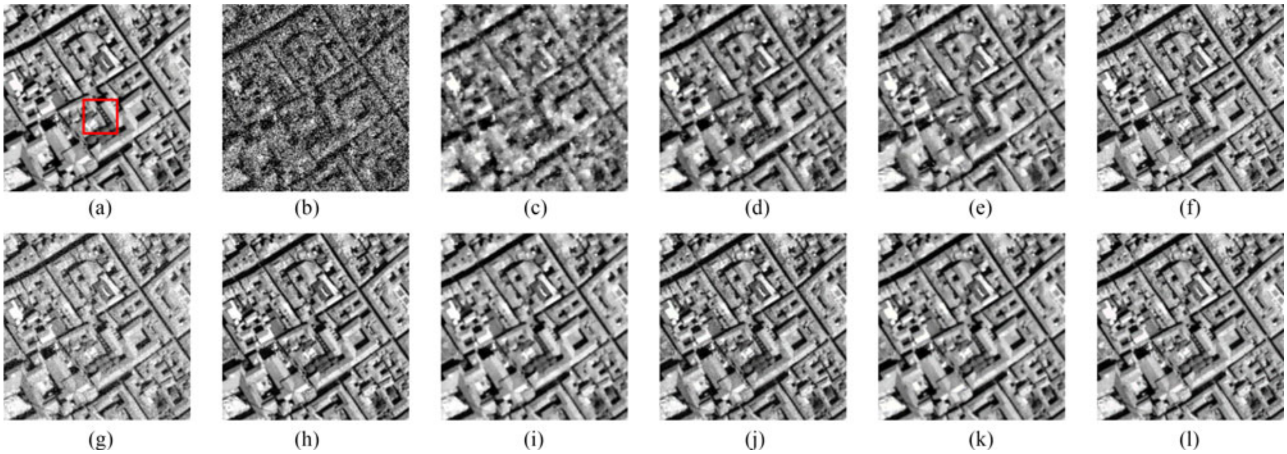

Fig. 14. Pavia city center image before and after denoising. (a) Original image of band 51. (b) Noisy image in case 3 (15.54 dB). The image denoising results of (c) SSAHTV (23.90 dB), (d) SSTV (25.96 dB), (e) BM4D (26.44 dB), (f) LRRSDS (35.01 dB), (g) NAILRMA (30.26 dB), (h) FastHyDe (34.11 dB), (i) LSSTV (33.57 dB), (j) LRMR (33.34 dB), (k) LRTV (34.30 dB), and (l) LLRSSTV (36.58 db).

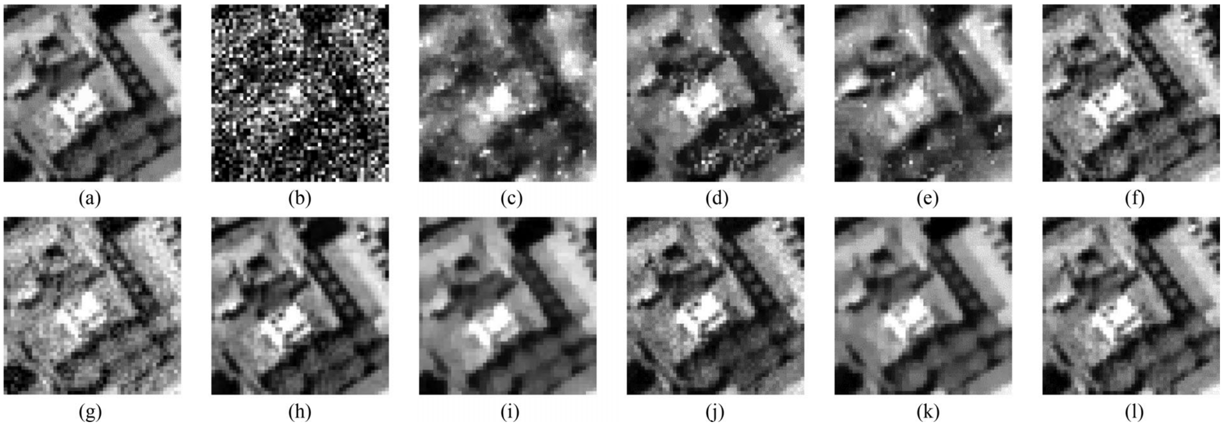

Fig. 15. Magnified results of Fig. 14. (a) Original band. (b) Noisy image. The image denoising results of (c) SSAHTV, (d) SSTV, (e) BM4D, (f) LRRSDS, (g) NAILRMA, (h) FastHyDe, (i) LSSTV, (j) LRMR, (k) LRTV, and (l) LLRSSTV.

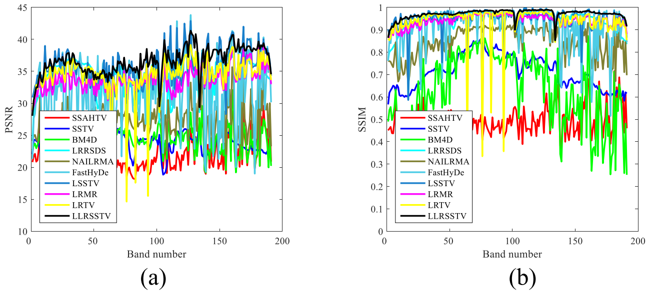

Fig. 16. PSNR and SSIM values of each band in the experiment with the Washington DC Mall image in case 3. (a) PSNR. (b) SSIM.

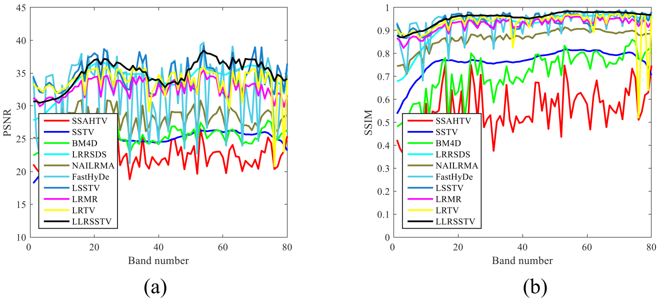

Fig. 17. PSNR and SSIM values of each band in the experiment with the Pavia city center image in case 3. (a) PSNR. (b) SSIM.

PSNR values of the three bands shown are labeled below the figure. Fig. 14 shows the results with the Pavia city center image. Figs. 13 and 15 present the magnified results of Figs. 12 and 14, respectively. From Figs. 12 to 15(c)–(e), it can be observed that SSAHTV, SSTV, and BM4D fail to remove the mixed noise. LRRSDS and LRMR can remove the sparse noise, but still leave some small amounts of noise in the experimental results. LSSTV and LRTV can obtain better results; unfortunately, they both smooth the details of the results, to some extent. As presented in Fig. 13(i) and (k), in the LSSTV and LRTV results, the cars along the road and the details on the roof are smoothed and blurred. A similar phenomenon also appears in Fig. 15(i) and (k). From these figures, it can be observed that the proposed LLRSSTV is best able to preserve the local details and remove the noise.

We also show the PSNR and SSIM values of each band of the Washington DC Mall and Pavia city center images in the case 3 experiments in Figs. 16 and 17, respectively. As presented in the two figures, the proposed method achieves the best PSNR and SSIM values in most bands of the image, which further demonstrates the superiority of the proposed LLRSSTV method.

B. Real HSI Data Experiments

In this section, we present the experimental results obtained with three real datasets.

1) AVIRIS Indian Pines Dataset: The Indian Pines dataset[4] was acquired by the NASA airborne visible/infrared imaging spectrometer (AVIRIS) instrument over the Indian Pines test site in Northwestern Indiana in 1992. The data size is 145 × 145 pixels and 220 bands. Some bands of the dataset are heavily corrupted with mixed Gaussian and impulse noise, while the other bands are of high quality. The purpose of the Indian Pines dataset denoising is to remove the noise in the noisy bands and preserve the details of the high-quality bands.

Figs. 18 and 19 show the images of bands 150 and 220 before and after denoising via the different methods. It can be clearly observed that SSAHTV, SSTV, and BM4D fail to restore the details of bands 150 and 220. BM4D can recover some of the artifacts, as shown in Fig. 19(d). LRRSDS, NAILRMA, and LRMR can more or less remove the noise, but the denoising results are not complete, as presented in Fig. 19(e), (f), and (h), which still show some noise remaining. LSSTV and LRTV are moderately effective at removing the noise. However, they also smooth the details, as marked by the red circle shown in Fig. 19. To sum up, FastHyDe and the proposed LLRSSTV achieve the best denoising results, removing most of the noise while preserving most of the details of the image. In Table II, we also provide a blind image quality assessment, as introduced in [54],[5] [5] to evaluate

---

[4] Available: https://engineering.purdue.edu/∼biehl/MultiSpec/hyperspectral.html

[5] The MATLAB code was provided by Dr. Jingxiang Yang

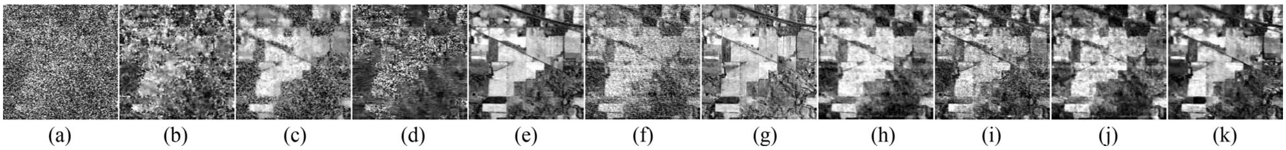
(a) (b) (c) (d) (e) (f) (g) (h) (i) (j) (k)

Fig. 18. Band 150 of the Indian Pines dataset before and after denoising via the different methods. (a) Original image of band 150. Image denoising results of (b) SSAHTV, (c) SSTV, (d) BM4D, (e) LRRSDS, (f) NAILRMA, (g) FastHyDe, (h) LSSTV, (i) LRMR, (j) LRTV, and (k) LLRSSTV.

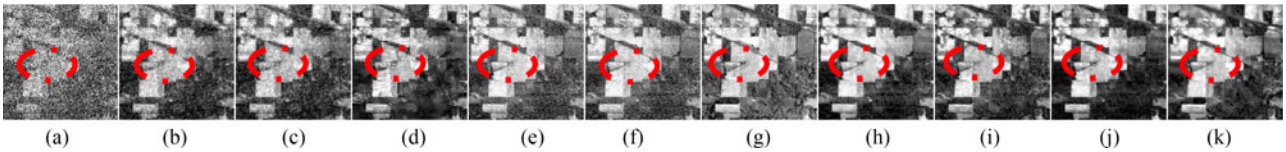
(a) (b) (c) (d) (e) (f) (g) (h) (i) (j) (k)

Fig. 19. Band 220 of the Indian Pines dataset before and after denoising via the different methods. (a) Original image of band 220. Image denoising results of (b) SSAHTV, (c) SSTV, (d) BM4D, (e) LRRSDS, (f) NAILRMA, (g) FastHyDe, (h) LSSTV, (i) LRMR, (j) LRTV, and (k) LLRSSTV.

TABLE II
BLIND HYPERSPECTRAL IMAGE QUALITY ASSESSMENT ON THE INDIAN PINES IMAGE

Method	SSAHTV	SSTV	BM4D	LRRSDS	NAILRMA	FastHyDe	LSSTV	LRMR	LRTV	LLRSSTV
Score	17.95	18.95	16.26	16.11	16.16	16.14	15.67	17.04	15.79	14.89

the images before and after denoising. A better denoising result is indicated by a lower blind image quality assessment score [54]. As shown in this table, the proposed LLRSSTV method achieves the lowest score, further demonstrating the superiority of LLRSSTV.

2) EO-1 Hyperion Dataset: The second real dataset used in the experiments was the EO-1 Hyperion hyperspectral dataset [55], which covers an agricultural area of the state of Indiana, USA. The original data have 242 bands spanning 0.35–2.6 μm. After removing blank bands, 192 bands were retained, and a subimage of 150 × 150 was adopted to implement the experiment. The EO-1 Hyperion data are heavily contaminated by stripes and impulse noise, which can be categorized as sparse noise.

Figs. 20 and 21 show the denoising results obtained with the EO-1 Hyperion data of bands 116 and 195, respectively. These two bands are heavily contaminated by stripes. Both LRTV and LLRSSTV can effectively remove the stripes. From another aspect, FastHyDe and the proposed LLRSSTV can better preserve the details, as marked by the red circle in Fig. 21, while the other comparison methods cannot. In addition, the stripes still exist in the other denoising results, as shown in Figs. 21 and 22(b)–(h). To further demonstrate the effect of the proposed LLRSSTV, we also present the vertical mean profiles of band 116 of the EO-1 data before and after denoising in Fig. 22. As shown in Fig. 22, the horizontal axis is the column number, and the vertical axis represents the mean digital number value of each column. Typically, the mean profiles are assumed to be smooth. Unfortunately, there are rapid fluctuations in the curve of the original observation image, due to the stripes. After denoising, this kind of fluctuation can be effectively suppressed. From Fig. 22, we can observe that the proposed LLRSSTV can obtain a smoother vertical mean profile, indicating the best destriping performance in the EO-1 Hyperion experiment.

3) HYDICE Urban Dataset: The HYDICE Urban dataset was adopted in the third real data experiment. The original image is 307 × 307 × 210 in size, and we selected a subimage of 200 × 200 × 210 for our experiment. Figs. 23 and 24 show the images of bands 139 and 206 before and after denoising. Horizontal stripes exist in most bands of the Urban dataset and can be regarded as a textural feature of the image from a spectral perspective. The TV-based method can remove this kind of striping, to some extent. However, it also results in over-smoothing of the image, as presented in Fig. 24(b). LRRSDS, FastHyDe, LSSTV, LRTV, and LLRSSTV achieve good destriping results. However, LRTV and LSSTV also lose a lot of details, as presented in Fig. 23(g) and (f). From another aspect, FastHyDe and the proposed LLRSSTV can both effectively remove the stripes and preserve the local details of the image.

C. Discussion

The running time is an effective way to measure the efficiency of a denoising method. For each iteration of the proposed method, the computational burden consists of two parts, i.e., local low-rank and sparse matrix decomposition and global SSTV-regularized image reconstruction. The global SSTV-regularized image reconstruction is accelerated by FFT. The local low-rank and sparse matrix decomposition can be computed by SVD and a shrinkage operation. The running times of the different methods on the three real image datasets are presented in Table III. All the experiments were conducted in MATLAB 2014a on the same personal computer with an Intel i7 CPU at 2.60 GHz and 12 GB of memory. The proposed method could also be further

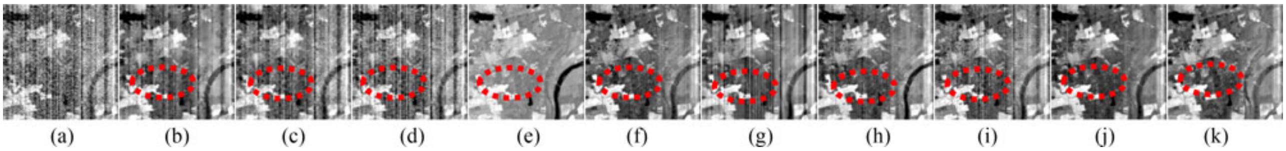

Fig. 20. Band 116 of the EO-1 Hyperion dataset before and after denoising via the different methods. (a) Original image of band 116. Image denoising results of (b) SSAHTV, (c) SSTV, (d) BM4D, (e) LRRSDS, (f) NAILRMA, (g) FastHyDe, (h) LSSTV, (i) LRMR, (j) LRTV, and (k) LLRSSTV.

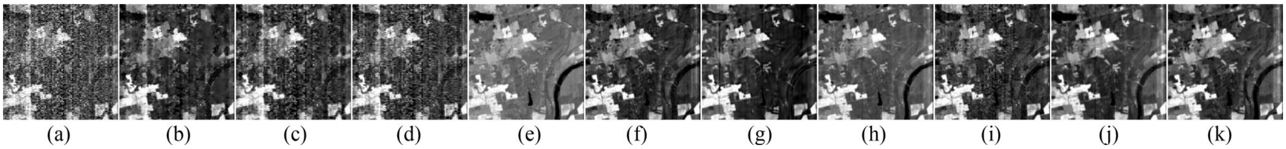

Fig. 21. Band 195 of the EO-1 Hyperion dataset before and after denoising via the different methods. (a) Original image of band 195. Image denoising results of (b) SSAHTV, (c) SSTV, (d) BM4D, (e) LRRSDS, (f) NAILRMA, (g) FastHyDe, (h) LSSTV, (i) LRMR, (j) LRTV, and (k) LLRSSTV.

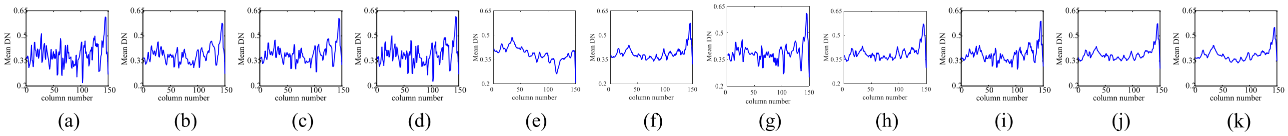

Fig. 22. Vertical mean profiles of band 116 in the real EO-1 Hyperion dataset experiment: (a) Original, (b) SSAHTV, (c) SSTV, (d) BM4D, (e) LRRSDS, (f) NAILRMA, (g) FastHyDe, (h) LSSTV, (i) LRMR, (j) LRTV, and (k) LLRSSTV.

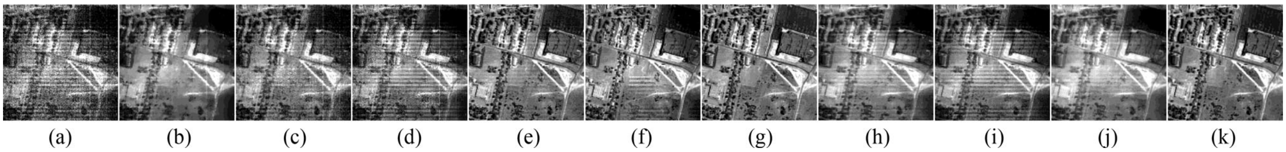

Fig. 23. Band 139 of the HYDICE Urban dataset before and after denoising via the different methods. (a) Original image of band 139. Image denoising results of (b) SSAHTV, (c) SSTV, (d) BM4D, (e) LRRSDS, (f) NAILRMA, (g) FastHyDe, (h) LSSTV, (i) LRMR, (j) LRTV, and (k) LLRSSTV.

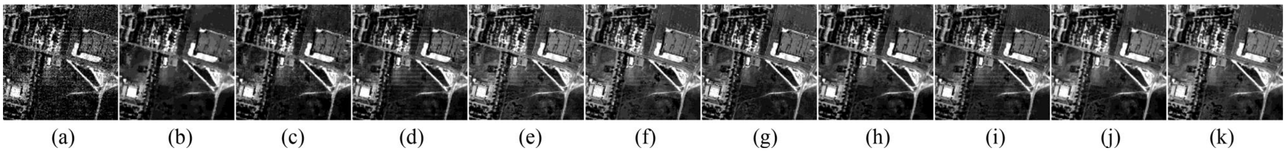

Fig. 24. Band 206 of the HYDICE Urban dataset before and after denoising via the different methods. (a) Original image of band 139. Image denoising results of (b) SSAHTV, (c) SSTV, (d) BM4D, (e) LRRSDS, (f) NAILRMA, (g) FastHyDe, (h) LSSTV, (i) LRMR, (j) LRTV, and (k) LLRSSTV.

TABLE III
RUNNING TIMES (IN SECONDS) OF THE DIFFERENT METHODS IN THE REAL HSI DATA EXPERIMENTS

HSI Data	SSAHTV	SSTV	BM4D	LRRSDS	NAILRMA	FastHyDe	LSSTV	LRMR	LRTV	LLRSSTV
AVIRIS Indian Pines	43	19	262	108	96	26	62	198	409	122
EO-1 Hyperion	29	15	252	89	81	22	49	138	327	93
HYDICE Urban	72	38	455	176	154	39	106	417	677	192

accelerated by parallel computing of the SVD of all the patches, which occupies the most time in each iteration.

Instead of providing the mathematical convergence proof, we present the convergence tendency of the LLRSSTV algorithm by experiment. Fig. 25 presents the evolutionary curve of the MPSNR values versus the iteration number of the proposed LLRSSTV in case 1 of the simulated experiments. From the figure, it can be clearly observed that the MPSNR values of the proposed method increase as the iteration progresses. In addition, the values become stable after only about ten iterations, indicating the good convergence behavior of the proposed method with the two experimental datasets.

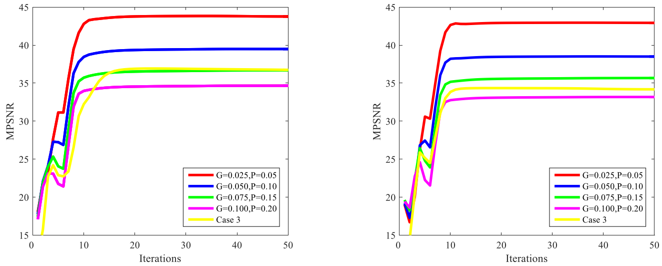

(a) (b)

Fig. 25. MPSNR values versus the iteration number of LLRSSTV with the two datasets in the simulated experiments of case 1. (a) The Washington DC Mall image. (b) The Pavia city center image.

V. CONCLUSION

Different types of noise have different statistical characteristics, and the existence of mixed noise in HSIs brings about great challenges for noise removal. In this paper, we have proposed an HSI mixed-noise removal method by simultaneously exploiting the local low-rank structure and the global spatial–spectral piecewise smoothness and consistency of the HSI. The HSI is divided into overlapping patches and each clean patch is assumed to be of local low rank. Differing from the previous low-rank-based approaches, which process all the patches individually, all the patches are updated together to separate the low-rank clean signal from the sparse and Gaussian noise. Notably, to further remove the Gaussian noise, a global SSTV regularization model is utilized to reconstruct the clean image. The SSTV-regularized image reconstruction can also preserve the global spatial–spectral smoothness of the HSI. In return, the reconstructed clean image is fed back to help the decomposition of the local clean patches and sparse noise. The proposed LLRSSTV method was tested on several HSIs, which confirmed the superiority of LLRSSTV, in both visual and quantitative assessments.

In the proposed LLRSSTV, we adopt matrix SVD to explore the low-rank structure of each patch. In fact, the divided patches can make up a tensor and, thus, the low-rank clean patches can be regarded as a low-rank tensor. In this way, the low-rank tensor based method could be adopted to complete the decomposition of the clean patches and noisy patches. In the future, we will incorporate tensor decomposition into our HSI denoising framework.

ACKNOWLEDGMENT

The authors would like to thank the anonymous editor and reviewers, who gave valuable comments and helped to improve the quality of the paper.

REFERENCES

[1] J. M. Bioucas-Dias *et al.*, "Hyperspectral unmixing overview: Geometrical, statistical, and sparse regression-based approaches," *IEEE J. Select. Topics Appl. Earth Observ. Remote Sens.*, vol. 5, no. 2, pp. 354–379, Apr. 2012.

[2] A. Ma, Y. Zhong, and B. Zhao, "Semisupervised subspace-based DNA encoding and matching classifier for hyperspectral remote sensing imagery," *IEEE Trans. Geosci. Remote Sens.*, vol. 54, no. 8, pp. 4402–4418, Aug. 2016.

[3] H. Zhang, H. Zhai, L. Zhang, and P. Li, "Spectral-spatial sparse subspace clustering for hyperspectral remote sensing images," *IEEE Trans. Geosci. Remote Sens.*, vol. 54, no. 6, pp. 3672–3684, Jun. 2016.

[4] S. Yang and Z. Shi, "Hyperspectral image target detection improvement based on total variation," *IEEE Trans. Image Process.*, vol. 25, no. 5, pp. 2249–2258, May 2016.

[5] Y. Chang, L. Yan, H. Fang, and C. Luo, "Anisotropic spectral-spatial total variation model for multispectral remote sensing image destriping," *IEEE Trans. Image Process.*, vol. 24, no. 6, pp. 1852–1866, Jun. 2015.

[6] C. Jiang, H. Zhang, L. Zhang, H. Shen, and Q. Yuan, "Hyperspectral image denoising with a combined spatial and spectral weighted hyperspectral total variation model," *Can. J. Remote Sens.*, vol. 42, no. 1, pp. 53–72, 2016.

[7] K. Dabov, A. Foi, V. Katkovnik, and K. Egiazarian, "Image denoising by sparse 3-D transform-domain collaborative filtering," *IEEE Trans. Image Process.*, vol. 16, no. 8, pp. 2080–2095, Aug. 2007.

[8] M. Elad and M. Aharon, "Image denoising via sparse and redundant representations over learned dictionaries," *IEEE Trans. Image Process.*, vol. 15, no. 12, pp. 3736–3745, Dec. 2006.

[9] J. Mairal, F. Bach, J. Ponce, G. Sapiro, and A. Zisserman, "Non-local sparse models for image restoration," in *Proc. IEEE 12th Int. Conf. Comput. Vision*, 2009, pp. 2272–2279.

[10] W. Dong, G. Shi, and X. Li, "Nonlocal image restoration with bilateral variance estimation: A low-rank approach," *IEEE Trans. Image Process.*, vol. 22, no. 2, pp. 700–711, Feb. 2013.

[11] M. Golbabaee, S. Arberet, and P. Vandergheynst, "Compressive source separation: Theory and methods for hyperspectral imaging," *IEEE Trans. Image Process.*, vol. 22, no. 12, pp. 5096–5110, Dec. 2013.

[12] H. K. Aggarwal and A. Majumdar, "Exploiting spatiospectral correlation for impulse denoising in hyperspectral images," *J. Electron. Imag.*, vol. 24, no. 1, 2015, Art. no. 013027.

[13] C.-I. Chang and Q. Du, "Interference and noise-adjusted principal components analysis," *IEEE Trans. Geosci. Remote Sens.*, vol. 37, no. 5, pp. 2387–2396, Sept. 1999.

[14] H. Zhang, W. He, L. Zhang, H. Shen, and Q. Yuan, "Hyperspectral image restoration using low-rank matrix recovery," *IEEE Trans. Geosci. Remote Sens.*, vol. 52, no. 8, pp. 4729–4743, Aug. 2014.

[15] W. He, H. Zhang, L. Zhang, and H. Shen, "Hyperspectral Image denoising via noise-adjusted iterative low-rank matrix approximation," *IEEE J. Select. Topics Appl. Earth Observ. Remote Sens.*, vol. 8, no. 6, pp. 3050–3061, Jun. 2015.

[16] Y. Qian and M. Ye, "Hyperspectral imagery restoration using nonlocal spectral-spatial structured sparse representation with noise estimation," *IEEE J. Select. Topics Appl. Earth Observ. Remote Sens.*, vol. 6, no. 2, pp. 499–515, Apr. 2013.

[17] H. Othman and S.-E. Qian, "Noise reduction of hyperspectral imagery using hybrid spatial-spectral derivative-domain wavelet shrinkage," *IEEE Trans. Geosci. Remote Sens.*, vol. 44, no. 2, pp. 397–408, Feb. 2006.

[18] W. He, H. Zhang, L. Zhang, and H. Shen, "A noise-adjusted iterative randomized singular value decomposition method for hyperspectral image denoising," in *Proc. 2014 IEEE Geosci. Remote Sens. Symp.*, Quebec, ON, Canada, 2014, pp. 1536–1539.

[19] W. He, H. Zhang, and L. Zhang, "Total variation regularized reweighted sparse nonnegative matrix factorization for hyperspectral unmixing," *IEEE Trans. Geosci. Remote Sens.*, vol. 55, no. 7, pp. 3909–3921, Apr. 2017.

[20] J. Li, Q. Yuan, H. Shen, and L. Zhang, "Noise removal from hyperspectral image with joint spectral-spatial distributed sparse representation," *IEEE Trans. Geosci. Remote Sens.*, vol. 54, no. 9, pp. 5425–5439, Sept. 2016.

[21] E. J. Candès, X. Li, Y. Ma, and J. Wright, "Robust principal component analysis?" *J. ACM*, vol. 58, no. 3, May 2011, Art. no. 11.

[22] P. Blomgren and T. F. Chan, "Color TV: Total variation methods for restoration of vector-valued images," *IEEE Trans. Image Process.*, vol. 7, no. 3, pp. 304–309, Mar. 1998.

[23] Q. Yuan, L. Zhang, and H. Shen, "Hyperspectral image denoising employing a spectral-spatial adaptive total variation model," *IEEE Trans. Geosci. Remote Sens.*, vol. 50, no. 10, pp. 3660–3677, Oct. 2012.

[24] L. Zhuang and J. M. Bioucas-Dias, "Fast hyperspectral image denoising based on low rank and sparse representations," in *Proc. 2016 IEEE Int. Geosci. Remote Sens. Symp.*, 2016, pp. 1847–1850.

[25] S. H. Chan, R. Khoshabeh, K. B. Gibson, P. E. Gill, and T. Q. Nguyen, "An augmented Lagrangian method for total variation video restoration," *IEEE Trans. Image Process.*, vol. 20, no. 11, pp. 3097–3111, Nov. 2011.

[26] L. Zhang, W. Dong, D. Zhang, and G. Shi, “Two-stage image denoising by principal component analysis with local pixel grouping,” *Pattern Recogn.*, vol. 43, no. 4, pp. 1531–1549, 2010.

[27] W. He, H. Zhang, and L. Zhang, “Sparsity-regularized robust non-negative matrix factorization for hyperspectral unmixing,” *IEEE J. Select. Topics Appl. Earth Observ. Remote Sens.*, vol. 9, no. 9, pp. 4267–4279, Sept. 2016.

[28] X. Liu, S. Bourennane, and C. Fossati, “Denoising of hyperspectral images using the PARAFAC model and statistical performance analysis,” *IEEE Trans. Geosci. Remote Sens.*, vol. 50, no. 10, pp. 3717–3724, Oct. 2012.

[29] Y. Chang, L. Yan, T. Wu, and S. Zhong, “Remote sensing image stripe noise removal: From image decomposition perspective,” *IEEE Trans. Geosci. Remote Sens.*, vol. 54, no. 12, pp. 7018–7031, Dec. 2016.

[30] X. Cao *et al.*, “Low-rank matrix factorization under general mixture noise distributions,” in *Proc. 2015 IEEE Int. Conf. Comput. Vision*, 2015, pp. 1493–1501.

[31] Q. Zhao *et al.*, “A novel sparsity measure for tensor recovery,” in *Proc. 2015 IEEE Int. Conf. Comput. Vision*, 2015, pp. 271–279.

[32] X. Lu, Y. Wang, and Y. Yuan, “Graph-regularized low-rank representation for destriping of hyperspectral images,” *IEEE Trans. Geosci. Remote Sens.*, vol. 51, no. 7, pp. 4009–4018, Jul. 2013.

[33] G. Chen and S.-E. Qian, “Denoising of hyperspectral imagery using principal component analysis and wavelet shrinkage,” *IEEE Trans. Geosci. Remote Sens.*, vol. 49, no. 3, pp. 973–980, Mar. 2011.

[34] B. Rasti, J. R. Sveinsson, and M. O. Ulfarsson, “Wavelet-based sparse reduced-rank regression for hyperspectral image restoration,” *IEEE Trans. Geosci. Remote Sens.*, vol. 52, no. 10, pp. 6688–6698, Oct. 2014.

[35] W. He, H. Zhang, L. Zhang, and H. Shen, “Total-variation-regularized low-rank matrix factorization for hyperspectral image restoration,” *IEEE Trans. Geosci. Remote Sens.*, vol. 54, no. 1, pp. 178–188, Jan. 2016.

[36] Y.-Q. Zhao and J. Yang, “Hyperspectral image denoising via sparse representation and low-rank constraint,” *IEEE Trans. Geosci. Remote Sens.*, vol. 53, no. 1, pp. 296–308, Jan. 2015.

[37] Q. Wang, Z. Wu, J. Jin, T. Wang, and Y. Shen, “Low rank constraint and spatial spectral total variation for hyperspectral image mixed denoising,” *Signal Process.*, vol. 142, pp. 11–26, 2018.

[38] Y. Xie, Y. Qu, D. Tao, W. Wu, Q. Yuan, and W. Zhang, “Hyperspectral image restoration via iteratively regularized weighted Schatten p-norm minimization,” *IEEE Trans. Geosci. Remote Sens.*, vol. 54, no. 8, pp. 4642–4659, Aug. 2016.

[39] T. Lu, S. Li, L. Fang, Y. Ma, and J. A. Benediktsson, “Spectral-spatial adaptive sparse representation for hyperspectral image denoising,” *IEEE Trans. Geosci. Remote Sens.*, vol. 54, no. 1, pp. 373–385, Jan. 2016.

[40] Y. Xu, Z. Wu, and Z. Wei, “Spectral-spatial classification of hyperspectral image based on low-rank decomposition,” *IEEE J. Select. Topics Appl. Earth Observ. Remote Sens.*, vol. 8, no. 6, pp. 2370–2380, Jun. 2015.

[41] Y. Peng, D. Meng, Z. Xu, C. Gao, Y. Yang, and B. Zhang, “Decomposable nonlocal tensor dictionary learning for multispectral image denoising,” in *Proc. 2014 IEEE Conf. Comput. Vision Pattern Recogn.*, 2014, pp. 2949–2956.

[42] W. Dong, G. Li, G. Shi, X. Li, and Y. Ma, “Low-rank tensor approximation with Laplacian scale mixture modeling for multiframe image denoising,” in *Proc. 2015 IEEE Int. Conf. Comput. Vision*, 2015, pp. 442–449.

[43] X. Ding, L. He, and L. Carin, “Bayesian robust principal component analysis,” *IEEE Trans. Image Process.*, vol. 20, no. 12, pp. 3419–3430, Dec. 2011.

[44] G. Liu, Z. Lin, S. Yan, J. Sun, Y. Yu, and Y. Ma, “Robust recovery of subspace structures by low-rank representation,” *IEEE Trans. Pattern Anal. Mach. Intell.*, vol. 35, no. 1, pp. 171–184, Jan. 2013.

[45] R. Mazumder, T. Hastie, and R. Tibshirani, “Spectral regularization algorithms for learning large incomplete matrices,” *J. Mach. Learn. Res.*, vol. 99, pp. 2287–2322, 2010.

[46] E. J. Candes, C. A. Sing-Long, and J. D. Trzasko, “Unbiased risk estimates for singular value thresholding and spectral estimators,” *IEEE Trans. Signal Process.*, vol. 61, no. 19, pp. 4643–4657, Oct. 2013.

[47] L. Sun, Y. Zheng, and B. Jeon, “Hyperspectral restoration employing low rank and 3d total variation regularization,” in *Proc. IEEE Int. Conf. Prog. Informat. Comput.*, Dec. 2016, pp. 326–329.

[48] L. Sun, B. Jeon, Y. Zheng, and Z. Wu, “Hyperspectral image restoration using low-rank representation on spectral difference image,” *IEEE Geosci. Remote Sens. Lett.*, vol. 14, no. 6, pp. 1151–1155, Jul. 2017.

[49] J.-F. Cai, E. J. Candès, and Z. Shen, “A singular value thresholding algorithm for matrix completion,” *SIAM J. Optim.*, vol. 20, no. 4, pp. 1956–1982, Mar. 2010.

[50] Z. Lin, M. Chen, and Y. Ma, “The augmented lagrange multiplier method for exact recovery of corrupted low-rank matrices,” Univ. Illinois Urbana-Champaign, Champaign, IL, USA, Tech. Rep. UILU-ENG-09- 2215, 2009, Arxiv preprint arXiv:1009.5055.

[51] J. M. Bioucas-Dias and J. M. Nascimento, “Hyperspectral subspace identification,” *IEEE Trans. Geosci. Remote Sens.*, vol. 46, no. 8, pp. 2435–2445, Aug. 2008.

[52] M. Maggioni, V. Katkovnik, K. Egiazarian, and A. Foi, “Nonlocal transform-domain filter for volumetric data denoising and reconstruction,” *IEEE Trans. Image Process.*, vol. 22, no. 1, pp. 119–133, Jan. 2013.

[53] Z. Wang, A. C. Bovik, H. R. Sheikh, and E. P. Simoncelli, “Image quality assessment: From error visibility to structural similarity,” *IEEE Trans. Image Process.*, vol. 13, no. 4, pp. 600–612, Apr. 2004.

[54] J. Yang, Y. Zhao, C. Yi, and J. C.-W. Chan, “No-reference hyperspectral image quality assessment via quality-sensitive features learning,” *Remote Sens.*, vol. 9, no. 4, 2017, Art. no. 305.

[55] R. Zhao, B. Du, and L. Zhang, “Beyond background feature extraction: An anomaly detection algorithm inspired by slowly varying signal analysis,” *IEEE Trans. Geosci. Remote Sens.*, vol. 54, no. 3, pp. 1757–1774, Mar. 2016.

[56] L. I. Rudin, S. Osher, and E. Fatemi, “Nonlinear total variation based noise removal algorithms,” *Physica D* vol. 60, nos. 1–4, pp. 259–268, 1992.

Wei He (S’14–M’17) received the B.S. degree in mathematics and the Ph.D. degree in photogrammetry and remote sensing from Wuhan University,Wuhan, China, in 2012 and 2017, respectively.

He is currently a Researcher with the Geoinformatics Unit, RIKEN Center for Advanced Intelligence Project, Tokyo, Japan. His research interests include image quality improvement, remote sensing image processing, and low-rank representation.

Hongyan Zhang (M’13–SM’16) received the B.S. degree in geographic information system and the Ph.D. degree in photogrammetry and remote sensing from Wuhan University, Wuhan, China, in 2005 and 2010, respectively.

He has been currently a Full Professor with the State Key Laboratory of Information Engineering in Surveying, Mapping, and Remote Sensing, Wuhan University, since 2016. He has authored/co-authored more than 70 research papers. His research interests include image reconstruction for quality improvement, hyperspectral image processing, sparse representation, and low-rank methods for sensing image imagery.

Dr. Zhang currently serves as an Associate Editor for the *Computers and Geosciences Journal*. He is a Reviewer for more than 30 international academic journals, including the IEEE Transaction on Geoscience and Remote Sensing, the IEEE Transaction on Image Processing, the IEEE Journal of Selected Topics in Applied Earth Observations and Remote Sensing, the IEEE Geoscience and Remote Sensing Letters, and so on.

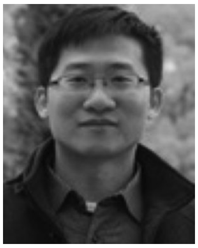

Huanfeng Shen (M’11–SM’13) received the B.S. degree in surveying and mapping engineering and the Ph.D. degree in photogrammetry and remote sensing from Wuhan University, Wuhan, China, in 2002 and 2007, respectively.

From 2006 to 2007, he was a Research Assistant with the Department of Mathematics, Hong Kong Baptist University. In July 2007, he joined the School of Resource and Environmental Sciences, Wuhan University, where he is currently a Luojia Distinguished Professor. He has authored or co-authored more than 100 research papers in international journals. His research interests include image quality improvement, remote sensing mapping and application, data fusion and assimilation, and regional and global environmental change.

Dr. Shen was or is the Principal Investigator (PI) for five National Natural Science Foundation of China projects, and a project PI for the National Key Research and Development Program of China. He has been supported by several China talent programs, such as The Youth Talent Support Program of China (2015), China National Science Fund for Excellent Young Scholars (2014), and the New Century Excellent Talents by the Ministry of Education of China (2011). He is a Council Member of the China Association of Remote Sensing Application. He is also currently a Member of the Editorial Board of the *Journal of Applied Remote Sensing*.

Liangpei Zhang (M'06–SM'08) received the B.S. degree in physics from Hunan Normal University, Changsha, China, in 1982, the M.S. degree in optics from Xi'an Institute of Optics and Precision Mechanics, Chinese Academy of Sciences, Xi'an, China, in 1988, and the Ph.D. degree in photogrammetry and remote sensing from Wuhan University, Wuhan, China, in 1998.

He is currently the Head of the Remote Sensing Division, State Key Laboratory of Information Engineering in Surveying, Mapping and Remote Sensing, Wuhan University. He is also a Chang-Jiang Scholar Chair Professor appointed by the Ministry of Education of China. He is currently a Principal Scientist for the China State Key Basic Research Project (2011–2016) appointed by the Ministry of National Science and Technology of China to lead the remote sensing program in China. He has more than 500 research papers and five books. He is the holder of 15 patents. His research interests include hyperspectral remote sensing, high-resolution remote sensing, image processing, and artificial intelligence.

Dr. Zhang is the Founding Chair of the IEEE Geoscience and Remote Sensing Society (GRSS) Wuhan Chapter. He is a Fellow of the Institution of Engineering and Technology, an Executive Member (Board of Governors) of the China National Committee of the International Geosphere–Biosphere Programme, an Executive Member of the China Society of Image and Graphics, etc. He regularly serves as a Co-Chair of the series International Society for Optics and Photonics Conferences on Multispectral Image Processing and Pattern Recognition, the Conference on Asia Remote Sensing, and many other conferences. He edits several conference proceedings, issues, and geoinformatics symposiums. He also serves as an Associate Editor for the *International Journal of Ambient Computing and Intelligence*, the *International Journal of Image and Graphics*, the *International Journal of Digital Multimedia Broadcasting*, the *Journal of Geo-Spatial Information Science*, the *Journal of Remote Sensing*, and the IEEE TRANSACTIONS ON GEOSCIENCE AND REMOTE SENSING. He is a Guest Editor for the *Journal of Applied Remote Sensing* and the *Journal of Sensors*. He was the General Chair for the Fourth IEEE GRSS Workshop on Hyperspectral Image and Signal Processing: Evolution in Remote Sensing and a Guest Editor for the IEEE JOURNAL OF SELECTED TOPICS IN APPLIED EARTH OBSERVATIONS AND REMOTE SENSING (JSTARS). He was the recipient of the Best Reviewer Awards from the IEEE GRSS for his service to the IEEE JSTARS in 2012 and the IEEE GEOSCIENCE AND REMOTE SENSING LETTERS in 2014. He was also the recipient of the 2010 Best Paper Boeing Award and the 2013 Best Paper ERDAS Award from the American Society of Photogrammetry and Remote Sensing. His research teams were the recipient of the top three prizes of the IEEE GRSS 2014 Data Fusion Contest, and his students have been selected as the winners or finalists of the IEEE International Geoscience and Remote Sensing Symposium Student Paper Contest in recent years.